6. Nonuniform Domain Growth and Higher Dimensions

6.1 Nonuniform Domain Growth

Thus far our investigation and analysis has been restricted to situations in which the domain growth is uniform, determined for the one-dimensional problem by the local strain rate which is independent of position (but may depend on time, as for the linear and logistic growth cases studied in Chapter 4). However, as was discussed during the derivation of the model, it is possible and generally desirable to consider a domain which is growing with different rates at different localities. For many biological systems growth is restricted to some region of a tissue, or does not occur at a uniform rate throughout the region of interest. We wish to investigate the formation of pattern sequences in the reaction-diffusion model under nonuniform conditions. In particular we would like to know whether introducing weak nonuniformity (where there is slow quantitative change in the growth across the domain) disrupts the FD sequence, or whether the sequence is robust to such changes. Furthermore, we are interested in whether suitably chosen and sufficiently strong nonuniformity (such that one section of the domain is growing in a quite different manner or rate to another part) can produce reliable sequences other than frequency-doubling.

Nonuniformity in the domain growth introduces terms with explicit spatial dependence into the evolution equation. In its original formulation, and in most subsequent development, the theory of pattern formation in reaction-diffusion equations assumes homogeneity in parameters throughout the domain, for the good reason that DDI generates inhomogeneity where before there was none. Indeed, this is the source of much of the theoretical interest in such pattern forming instabilities. One exception is the analytical study of a reaction term with explicit space-dependence by Auchmuty and Nicolis [5] (see also the numerical simulations of Herschkowitz-Kaufman [49]). Also, the recent interest in the modelling of chemical pattern formation in gel reactors leads to the study of spatial gradients in certain reaction terms. In the Gel Strip reactor the feed of the reactants, held at fixed concentrations at the boundaries, establishes steady gradients across the domain of pattern formation. Theoretical studies prior to the experimental realisation of Turing patterns in gel reactors are given by Dewel and Borckmans [25] and modelling of the structures experimentally observed in these ramped systems is presented by Borckmans *et al.* [9] and Dulos *et al.* [34].

In several applications of the theory to problems in biological pattern formation, authors have considered some underlying spatial dependence. For example, Gierer and Meinhardt [41] include a shallow source gradient in their model for morphogenesis and regeneration in Hydra to orient patterns (by removing degeneracy in the spatial modes). Benson [7] and coauthors have demonstrated that inhomogeneous reaction-diffusion equations may generate patterns with continuously varying amplitude [77]

(see also [81]) and wavelength [8] when one or both diffusion parameters are varying in space. In our equations for nonuniform domain growth the spatially-dependent terms are small, due to the small parameter arising from the different timescales, and so we do not expect strong influence on the amplitude or wavelength of patterns generated by the model.

Biologically there may be many underlying reasons for nonuniformity in domain growth. For example, signalling cues which determine the local growth rates (such as growth factors, or other chemicals) may not be uniformly distributed throughout the tissue. In such cases the local strain rate for the one-dimensional problem will depend on position (as well as time). In a simplified scenario for nonuniform growth, the domain comprises a number of subdomains each of which is undergoing growth at a different constant strain rate. Below we consider pattern formation for piece-wise uniform domain growth with two adjoining subdomains. Also, it is biological plausible that the reacting and diffusing chemicals may themselves be responsible for the local determination of the growth, so that the local expansion rate is a function of their concentrations, that is,

$$S(x,t) = S\big(\{c_i(x,t)\}\big), \quad i = 1, \ldots, n \tag{6.1}$$

a situation we call reactant-controlled growth.

The general reaction-diffusion model for nonuniform growth in one dimension is given by equation (3.31). Scaling the spatial dependence to the unit interval, writing $\xi = x/\ell(t) \in [0,1]$ for nondimensional domain length $\ell(t)$, we recover the evolution equations for two species $u(\xi,t)$ and $v(\xi,t)$

$$u_t = \frac{1}{\gamma(t)} u_{\xi\xi} + \chi(\xi,t)\, u_\xi + f(u,v) - S(\xi,t)\, u \tag{6.2}$$

$$v_t = \frac{d}{\gamma(t)} v_{\xi\xi} + \chi(\xi,t)\, v_\xi + g(u,v) - S(\xi,t)\, v \tag{6.3}$$

where $\gamma(t) = \gamma_0 \left[\ell\,(t)\right]^2$ and

$$\chi(\xi,t) = \frac{1}{\ell(t)} \Big[\xi\, \dot{\ell}(t) - a(\xi,t)\Big] \tag{6.4}$$

(where the dot represents a time derivative). Local growth $S(\xi,t)$ determines the local velocity field $a(\xi,t)$ via equation (3.27). Generally S is specified in terms of the Lagrangian variables (X,t). The position x of a particle at time t originally at position X at time $t = 0$ is given by $x = \Gamma(X,t)$, so that the uniformly scaled position $\xi = \Gamma(X,t)/\ell(t)$. To calculate S we must be able to compute the value of X corresponding to particular ξ and t (hence we are required to invert Γ).

6.1.1 Piece-wise Uniform Domain Growth. To investigate the role of nonuniformity in the domain growth we firstly consider the example of a one-dimensional domain comprising two subdomains undergoing slow uniform domain growth but with

different (slow) growth rates. This problem is studied in detail with the aim of gaining insight into the possibilities and complexities of pattern sequence formation under more general nonuniform growth conditions.

For slow uniform growth, from equation (3.61) we have $S(t) = \rho\sigma(t)$ giving the global growth function

$$x = \Gamma(X,t) = Xr(t) \tag{6.5}$$

where

$$r(t) = \exp\left[\rho\int_0^t \sigma(\bar{t})\,\mathrm{d}\bar{t}\right] \tag{6.6}$$

and for slow growth $0 < \rho \ll 1$. For the simplest example of piece-wise uniform domain growth we define S on the two subdomains by

$$S = S(t) = \begin{cases} S_1(t), & 0 \le X \le \Theta \\ S_2(t), & \Theta < X \le 1 \end{cases} \tag{6.7}$$

where Θ is the initial position of the interface between the two subdomains. For slow growth $S_i(t) = \rho\sigma_i(t)$, $i = 1,2$, and by straightforward calculation from equation (3.29) we recover

$$x = \Gamma(X,t) = \begin{cases} Xr_1(t), & 0 \le X \le \Theta \\ \Theta(r_1(t) - r_2(t)) + Xr_2(t), & \Theta < X \le 1 \end{cases} \tag{6.8}$$

where the r_i are calculated as in equation (6.6). Due to the growth of the left-hand subdomain ($i = 1$) the interface between the subdomains $\theta(t) \in [0, \ell(t)]$ moves as

$$\theta(t) = \Theta r_1(t) \tag{6.9}$$

and is a moving internal boundary. Similarly, from equation (3.33) along with the second of (6.8) the total domain length is given by

$$\ell(t) = \Theta r_1(t) + (1-\Theta)\, r_2(t) \tag{6.10}$$

and the rate of change $\dot{\ell}(t)$ follows accordingly. We may now calculate the flow, a, for the piece-wise uniform case from the expression for Γ, where $a = \partial\Gamma/\partial t$, giving

$$a(X,t) = \begin{cases} X\dot{r}_1(t), & 0 \le X \le \Theta \\ \Theta(\dot{r}_1(t) - \dot{r}_2(t)) + X\dot{r}_2(t), & \Theta < X \le 1 \end{cases}. \tag{6.11}$$

Writing as a function of x and t we have

$$a(x,t) = \begin{cases} x\dfrac{\dot{r}_1}{r_1}, & 0 \le x \le \theta(t) \\ \theta(t)\left(\dfrac{\dot{r}_1}{r_1} - \dfrac{\dot{r}_2}{r_2}\right) + x\dfrac{\dot{r}_2}{r_2}, & \theta(t) < x \le \ell(t) \end{cases} \tag{6.12}$$

and in the uniformly scaled coordinates (ξ, t)

$$\frac{a(\xi,t)}{\ell(t)} = \begin{cases} \xi\dfrac{\dot{r}_1}{r_1}, & 0 \le \xi \le \tilde{\theta}(t) \\ \tilde{\theta}(t)\left(\dfrac{\dot{r}_1}{r_1} - \dfrac{\dot{r}_2}{r_2}\right) + \xi\dfrac{\dot{r}_2}{r_2}, & \tilde{\theta}(t) < \xi \le 1 \end{cases} \tag{6.13}$$

where after the uniform scaling the interface between subdomains moves as $\tilde{\theta}(t) = \theta(t)/\ell(t) \in [0,1]$, which is easily written as a function of Θ, $r_1(t)$ and $r_2(t)$ only. Now we have all the components required to specify the evolution equations (6.2)–(6.2) for piece-wise uniform growth.[1]

We require the continuity of the solutions $u(\xi,t)$ and $v(\xi,t)$ and of their fluxes at the moving internal boundary $\xi = \tilde{\theta}(t)$ between the two subdomains. The diffusion constants are now effectively functions of time through $\gamma(t)$ but are independent of ξ and so continuity of flux requires that the first spatial derivative is continuous across $\xi = \tilde{\theta}(t)$ for each species. Thus we require at every time t

$$\Big[u(\xi,t)\Big]_{\tilde{\theta}^-(t)}^{\tilde{\theta}^+(t)} = 0, \qquad \Big[u_\xi(\xi,t)\Big]_{\tilde{\theta}^-(t)}^{\tilde{\theta}^+(t)} = 0 \tag{6.14}$$

and similarly for $v(\xi,t)$.

The advective terms in the equations arise despite the uniformity of growth for each subdomain because of the choice of spatial transformation, the differing growth rates necessitating the consideration of the internal moving boundary. A different approach to nondimensionalisation would consider two semi-domains, each transformed to the half-unit interval. Then there would be no moving boundary, the junction being fixed at $\xi = 1/2$, but the (time-dependent) diffusivities would be different on the two semi-domains. Clearly different spatial rescalings would be required for the two semi-domains in order to examine the form of the pattern on the dimensional domain, and these rescalings would change with time. This process would replace, and is equivalent to, the advective terms. The advective nature of the equations is thus rendered more transparent in the formulation chosen above which includes these terms explicitly.

For slow piece-wise uniform domain growth we must specify growth parameters $\rho \ll 1$ and Θ, and the initial domain size through γ_0 along with functions $\sigma_1(t)$ and $\sigma_2(t)$. We restrict discussion to the case where the σ_i are constant and to simplify notation we write

$$S_i = \rho_i, \quad i = 1,2 \tag{6.15}$$

where both ρ_1 and ρ_2 are of order ρ and hence are small parameters. Then $r_i(t)$ is given by the simple expression

$$r_i = \exp(\rho_i t), \quad i = 1,2 \tag{6.16}$$

[1] At each step in the discussion the equations reduce to the form derived for reaction-diffusion on a uniformly growing domain, equation (3.63), when the two subdomains have the same growth, i.e. when $\sigma_1(t) \equiv \sigma_2(t)$ such that $r_1(t) = r_2(t)$.

such that

$$\frac{a(\xi,t)}{\ell(t)} = \begin{cases} \rho_1 \xi, & 0 \le \xi \le \tilde{\theta}(t) \\ \tilde{\theta}(t)\,(\rho_1 - \rho_2) + \rho_2 \xi, & \tilde{\theta}(t) < \xi \le 1 \end{cases} . \tag{6.17}$$

For slow growth we notice that $a \sim \mathcal{O}(\rho)$ and, from equation (6.10) along with (6.16), that $\dot{\ell}(t) \sim \mathcal{O}(\rho)$. Given that $\ell(t) \ge 1$ and $\xi \in [0,1]$ we also find that $\chi \sim \mathcal{O}(\rho)$ or smaller, so that the advection component is small.

6.1.2 Numerical Solution for Slow Piece-wise Uniform Growth. Equations (6.2)–(6.4) along with (6.10) and (6.17) with initial data and boundary conditions at $\xi = 0, 1$ for both species, fully determine the problem to be solved numerically. The time-dependent internal boundary $\xi = \tilde{\theta}(t)$ introduces a further level of complexity into the numerical simulation of the system. We cannot simply reduce the problem to a set of ordinary differential equations by a naive spatial discretisation and standard central finite differences as the governing equations differ on the two subdomains. Therefore we must adapt the discretisation to incorporate the internal boundary.

The spatial interval is discretised with a uniform mesh, as for the uniform growth case, writing $U_i(t) \approx u(\xi_i, t)$ as the approximate values of the solution $u(\xi,t)$ at the mesh points ξ_i, $i = 1, 2, \ldots, N$, and similarly v is approximated by $V_i(t) \approx v(\xi_i, t)$. The first spatial derivative is taken as the standard central difference,

$$\frac{\partial u}{\partial \xi}(\xi_i, t) \approx \frac{U_{i+1}(t) - U_{i-1}(t)}{2h} \tag{6.18}$$

where h is the spatial mesh size. When this expression straddles the internal boundary the requirement of conservation of the first spatial derivative is invoked, and so the expression is universally valid on the interval. However, while central differences may also be used for the second spatial derivative within the two subdomains, the expression will not be valid across the internal boundary. Here we must adapt the expression when points in the central difference formula $\{\xi_{i-1}, \xi_i, \xi_{i+1}\}$ straddle the boundary $\tilde{\theta}(t)$. When this occurs we adopt the strategy often used to deal with conditions imposed on curved boundaries for finite differences (see Morton and Mayers [85]). We introduce an extra spatial mesh point, $\xi_\theta = \tilde{\theta}(t)$ at the internal boundary. When $\xi_i < \xi_\theta < \xi_{i+1}$ we proceed by calculating an approximation, U_θ, to the solution at position ξ_θ using linear interpolation between the approximations at points surrounding ξ_θ, given by U_i and U_{i+1}. Then we modify the central differences formula for the second derivative by foreshortening the range in the direction of the boundary

$$\begin{aligned} \left[\frac{\partial^2 u}{\partial \xi^2}\right]_{\xi_i} &\approx \frac{\left(\dfrac{U_\theta - U_i}{\xi_\theta - \xi_i}\right) - \left(\dfrac{U_i - U_{i-1}}{\xi_i - \xi_{i-1}}\right)}{\left(\dfrac{\xi_\theta - \xi_i}{2}\right) + \left(\dfrac{\xi_i - \xi_{i-1}}{2}\right)} \\ &= \frac{2}{\xi_\theta - \xi_{i-1}} \left[\left(\frac{U_\theta - U_i}{\xi_\theta - \xi_i}\right) - \left(\frac{U_i - U_{i-1}}{\xi_i - \xi_{i-1}}\right)\right] \end{aligned} \tag{6.19}$$

(omitting the time dependence for notational simplicity). A similar expression can be derived for the case $\xi_{i-1} < \xi_\theta < \xi_i$. Furthermore we approximate U_θ for $\xi_i < \xi_\theta < \xi_{i+1}$ by linear interpolation between the known points

$$\begin{aligned} U_\theta &\approx \frac{(\xi_{i+1} - \xi_\theta)}{h} U_i + \frac{(\xi_\theta - \xi_i)}{h} U_{i+1} \\ &= (1 - \lambda_+)\, U_i + \lambda_+ U_{i+1} \end{aligned} \tag{6.20}$$

where

$$\lambda_+ = \frac{\xi_\theta - \xi_i}{h}. \tag{6.21}$$

Then from the above we find the difference approximation for the second derivative

$$\left[\frac{\partial^2 u}{\partial \xi^2}\right]_{\xi_i} \approx \frac{2}{(1+\lambda)\, h^2} \left[U_{i+1} - 2U_i + U_{i-1}\right] \tag{6.22}$$

where $\lambda = \lambda_+$. The same expression is derived for the case $\xi_{i-1} < \xi_\theta < \xi_i$, where we have $\lambda = \lambda_-$ with

$$\lambda_- = \frac{\xi_i - \xi_\theta}{h}. \tag{6.23}$$

Using these expressions and similar expressions for v, and with appropriate conditions at the fixed boundaries $\xi = 0, 1$, we recover a system of ordinary differential equations in the U_i and V_i which may then be integrated in time with a suitable numerical routine, for example Gear's method, as employed for the uniform case.

Numerical Results. The results of numerical simulations under a variety of parameter regimes are presented below. Each of the two subdomains for piece-wise uniform growth undergoes spatially uniform exponential growth (at constant strain rate) such that if zero flux conditions were imposed at both ends of each subdomain then the frequency-doubling sequence would develop for both. However, the continuity of flux condition at the interface permits communication between the two regions. Pattern formation on each subdomain will influence the solution behaviour on the other. Thus we may expect that the pattern sequence will differ from the case of uniform exponential growth across the whole domain.

In Figure 6.1(a) we plot activator solutions for $\rho_1 = 0.01$, $\rho_2 = 0.02$ with $\gamma_0 = 1$, and with subdomains of initially equal length. In comparison to the pattern formed under uniform growth, as shown in Figure 6.1(b), the solution shows asymmetry in the temporal sequence of peak splitting and subsequently in the separation of peaks. The location of the interface between the uniformly growing subdomains is shown by the dashed line. In these and in subsequent figures the initial mode to form gives a boundary peak on the right hand boundary. Further numerical simulations have shown that the ensuing pattern sequence and asymmetry are the same for an initial peak located on the left-hand boundary. We have solved the uniform domain growth problem in Figure 6.1(b) using both the numerical scheme for the uniform equations (4.1)–(4.3) and for the piece-wise uniform growth formulation, and have found that the same

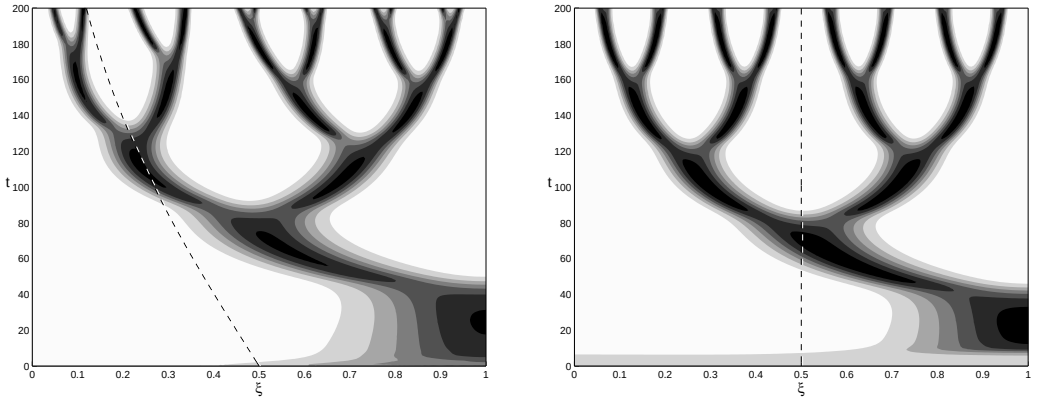

FIGURE 6.1 Asymmetric peak splitting for Schnakenberg kinetics on the piece-wise uniformly growing domain. Numerical solutions for the activator species $v(\xi, t)$ are shown for (a) piece-wise uniform domain growth with $\rho_1 = 0.01$, $\rho_2 = 0.02$ and $\gamma_0 = 1$ and (b) uniform domain growth with $\rho = 0.0172$ and $\gamma_0 = 1$ giving (approximately) the same dimensional domain length at time $t = 200$. The dashed line shows the interface $\tilde{\theta}(t)$ which is stationary for the uniform case. Shading is 0 (white) to 4 (black). In this and later figures we assume that the faster-growing subdomain is on the right hand side, however, this is for ease of comparison and is not required by the model formulation.

result is recovered in each case. The (stationary) location of the interface $\tilde{\theta} = 0.5$ is plotted for uniform growth as an aid to comparison. The activator concentration is plotted (in pseudo-colour, gray-scale) as a function of time and scaled spatial coordinate ξ, and therefore the relative separations of peaks on the dimensional domain at each time, found by uniform rescaling, are preserved.

At this relatively high value for the strain rate ρ the asymmetry in the peak splitting is reminiscent of the asymmetrical behaviour observed for the uniform growth case, described in section 4.2.2. Each peak in the activator concentration profile undergoes peak splitting and separation, and in this sense the evolving solution profile represents a perturbed frequency-doubling sequence. However, for slower domain growth peaks occasionally fail to undergo splitting, even when the growth rates on the two subdomains are in very close proximity. In Figure 6.2(a) the solution is plotted for $\rho_1 = 0.001$ and $\rho_2 = 0.0011$, for initially equal subdomain lengths. The solution follows closely the pattern for the uniform growth case, shown in Figure 6.2(b), until the 4-peak stage undergoes splitting at $t \approx 2500$, where the peak nearest the interface on the slower-growing subdomain fails to split. Subsequently the pattern reorganises so that the peak separation is again approximately equal across the whole domain. This defect in the peak splitting is reminiscent of the breakdown of the frequency doubling sequence for very slow uniform growth and for linear domain growth.

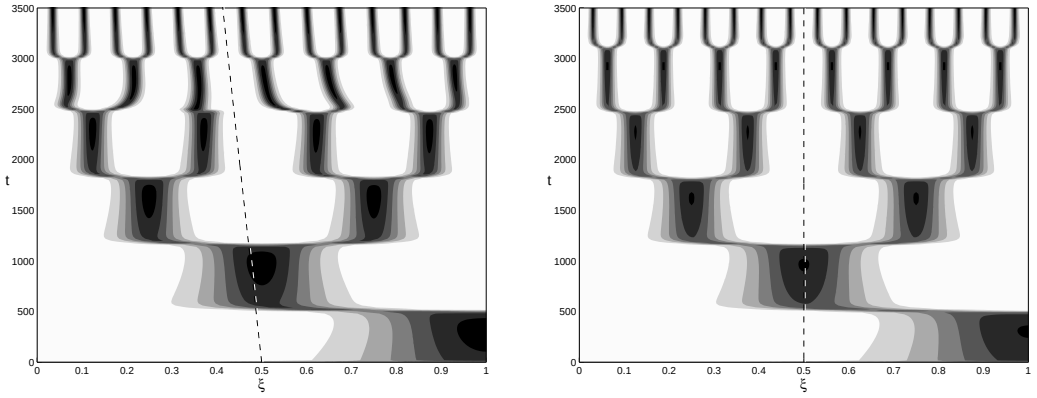

FIGURE 6.2 Missing peaks for piece-wise uniform domain growth. We plot numerical solutions for the activator $v(\xi, t)$ for (a) piece-wise uniform domain growth with $\rho_1 = 0.001$, $\rho_2 = 0.0011$ and $\gamma_0 = 1$ and (b) uniform domain growth with $\rho = 0.0010544$ and $\gamma_0 = 1$ giving (approximately) the same dimensional domain length at time $t = 3500$. Other remarks as for Figure 6.1.

When only one of the subdomains is growing, which may be considered to be an extreme case of the piece-wise uniform growth problem, then numerical simulations suggest that there is a strong tendency to peak splitting on the growing subdomain. This situation is illustrated in Figure 6.3(a), where $\rho_1 = 0$ and the initial domain size is such that the first pattern to form is the (right-hand) boundary peak. The FD-like pattern sequence which is generated has peaks restricted to the growing subdomain, and is asymmetric in a manner similar to the solution in Figure 6.1(a). For an initially left-hand boundary peak the same behaviour is found with all peaks moving into the growing region. If the initial domain size is increased so that patterns of higher mode are initially excited, then activator peaks may form simultaneously on the growing and non-growing subdomains, as shown in Figure 6.3(b) where the initial domain size was chosen to be $\gamma_0 = 20$. Here one can get different sequence behaviour. In the example, two peaks become three via splitting on the growing subdomain, and subsequently six peaks are formed, with peak splitting on the stationary subdomain close to the interface. However, the tendency for peaks to split on the growing part is retained.

When the growing subdomain has a slower growth rate the distinction between growing and non-growing regions appears even more distinct. In Figure 6.4(a) we plot the results of a repetition of the simulation in Figure 6.3(b), where we keep $\rho_1 = 0$ but take a smaller value for ρ_2. The transition from a two-peak pattern to three peaks is unambiguous and no peak splitting is observed on the non-growing part. However, the influence of the non-growing subdomain can be seen in the failure of peak splitting on the growing region later on. Similar results are found for an initial pattern of four peaks, shown for $\gamma_0 = 80$ in Figure 6.4(b).

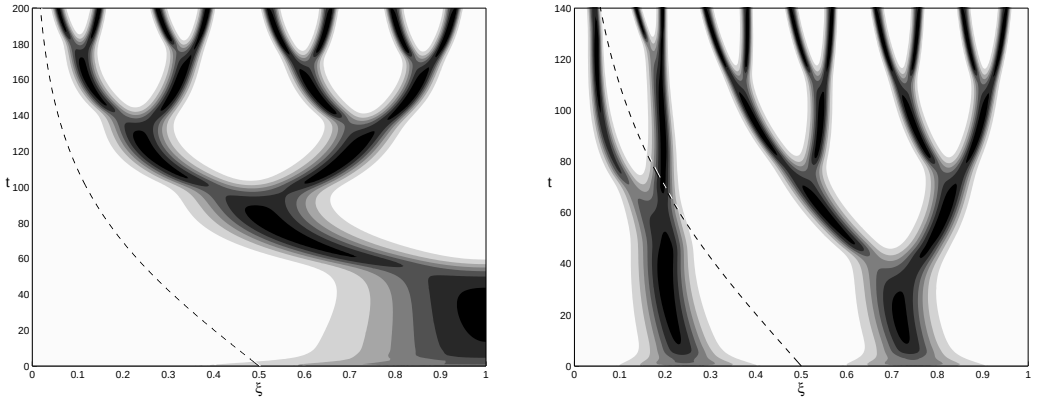

FIGURE 6.3 Pattern sequences generated from larger initial domains. We show the activator $v(\xi, t)$ for piece-wise uniform domain growth with $\rho_1 = 0.0$, $\rho_2 = 0.02$ and (a) $\gamma_0 = 1.0$ so that the initial mode $m = 1$ and (b) with $\gamma_0 = 20.0$ where the initial pattern is mode $m = 4$. Other remarks as for Figure 6.1.

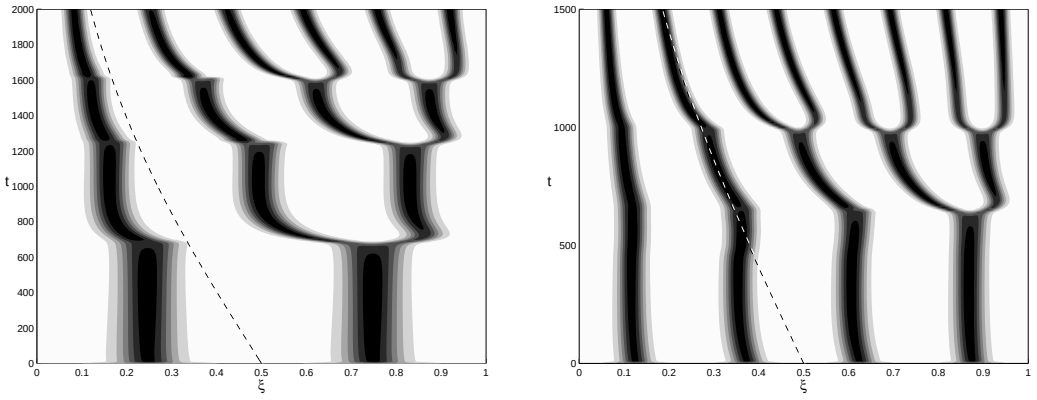

FIGURE 6.4 Pattern sequences generated from larger initial domains. Numerical solutions for activator $v(\xi, t)$ are shown for piece-wise uniform domain growth with $\rho_1 = 0.0$, $\rho_2 = 0.001$ and (a) $\gamma_0 = 20.0$ so that the initial mode to grow is mode $m = 4$ and (b) $\gamma_0 = 80.0$ where the initial pattern is $m = 8$. Other remarks as for Figure 6.1.

In this section we have considered only the example of Schnakenberg kinetics, and as a result we have discussed the consequences of piece-wise uniform domain growth for activator peak *splitting*. Similar results are found for kinetics which give rise to insertion of new activator peaks. In the following section we consider the problem for more general nonuniform domain growth which will provide a framework to validate the results we have presented for piece-wise uniform growth.

6.1.3 Lagrangian Formulation for Nonuniform Growth. The simple form of $\Gamma(X,t)$ for piece-wise uniform growth enabled us to invert Γ explicitly to find $X = \Lambda(x,t)$ and hence calculate a and S as functions of x and t. Λ can be found immediately for any uniform domain growth, where Γ is a separable function of X and t. For nonuniform growth the function Γ is not a separable function and it may not be possible to find Λ analytically. Therefore to compute numerical solutions for the evolution equations (6.2)–(6.3) it would be necessary to invert Γ numerically each time we require $a(\Lambda(x,t),t)$ and $S(\Lambda(x,t),t)$ during the computation. However, if the equations are recast in Lagrangian coordinates, (X,t), the inversion need only be performed when interpolating the results to find a solution at equally spaced ξ. In Lagrangian coordinates the evolution equation for $u(X,t)$ and $v(X,t)$ under nonuniform domain growth in one dimension with local growth $S(X,t)$ is given by

$$u_t = \frac{1}{\gamma_0}\frac{1}{\Gamma_X}\left[\frac{1}{\Gamma_X}u_X\right]_X + f(u,v) - Su \tag{6.24}$$

$$v_t = \frac{d}{\gamma_0}\frac{1}{\Gamma_X}\left[\frac{1}{\Gamma_X}v_X\right]_X + g(u,v) - Sv \tag{6.25}$$

$$[\Gamma_X]_t = S\,\Gamma_X \tag{6.26}$$

with zero flux boundary conditions for u and v and the zero translation boundary condition for Γ

$$u_X(X,t) = v_X(X,t) = 0, \quad X = 0,1 \tag{6.27}$$

$$\Gamma(0,t) = 0 \tag{6.28}$$

and initial conditions

$$u(X,0) = u_0(X), \qquad v(X,0) = v_0(X), \qquad \Gamma(X,0) = X. \tag{6.29}$$

These equations may be written as a system of first order PDEs in the variables $(u, u_X, v, v_X, \Gamma, \Gamma_X)$. Numerical solutions are found by discretising the first order system using the Keller box scheme [85], as implemented in the NAG library routine `D03PEF`. Solutions at equally spaced ξ or x may be calculated by interpolating from the solutions at equally spaced X, for example using routine `C05AZF` to invert Γ and `E01BFF` to interpolate.

We can use this more general formulation for solving the nonuniform domain growth equations to corroborate our results for piece-wise uniform domain growth. The function $S(X,t)$ we chose to approximate the step discontinuity in ρ across the

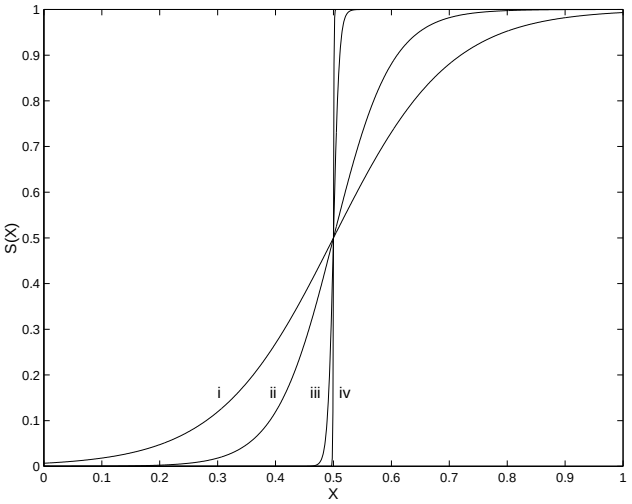

FIGURE 6.5 The *tanh* function, (6.30), illustrated for $S_1 = 0$ and $S_2 = 1$ with $\Theta = 0.5$ and (i) $\epsilon = 0.2$, (ii) $\epsilon = 0.1$, (iii) $\epsilon = 0.01$ and (iv) $\epsilon = 0.001$ showing successively closer approximations to a discontinuous step-function.

domain is the *tanh* function given by

$$S(X,t) = S_1(t) + \frac{S_2(t) - S_1(t)}{2}\left[1 + \tanh\left(\frac{X-\Theta}{\epsilon}\right)\right] \tag{6.30}$$

and shown in Figure 6.5, which as $\epsilon \to 0$ tends to a step-function between S_1 and S_2 (which may vary with time) centred on $X = \Theta$. In particular if we choose S_1 and S_2 to be constant, as in the previous case,

$$S_1(t) = \rho_1, \qquad S_2(t) = \rho_2 \tag{6.31}$$

then as $\epsilon \to 0$ we recover the piece-wise uniform S.

Numerical Results. Using the nonuniform equations with S given by (6.30) we can use the Lagrangian formulation to confirm our results for the piece-wise uniform case and to investigate the solution behaviour when there is a more gradual change of strain rate ρ over the domain.

For high values of the strain rate, i.e $\rho \sim 0.01$, there is little difference between the solutions for piece-wise uniform and nonuniform domain growth with smooth change in ρ across the domain, even when the change is very gradual ($\epsilon \sim 1$). As ρ is decreased we find that in the limit $\epsilon \to 0$ we recover the behaviour displayed on the piece-wise uniformly growing domain. Interestingly, it seems that certain of the features that we observed are dependent on the sharpness of the interface between subdomains for the piece-wise uniform case. In Figure 6.6 we plot activator solutions for decreasing ϵ corresponding to successively closer approximations to the piece-wise uniform problem, for which the corresponding solution is shown in Figure 6.2(a). When the change in S is gradual then all peaks undergo splitting (up to time $t = 3500$ at least), in a manner

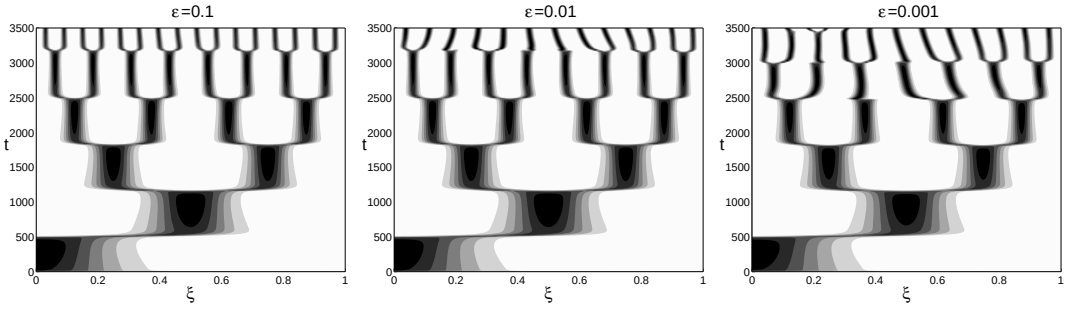

(a) (b) (c)

FIGURE 6.6 Pattern formation with nonuniform domain growth: as ϵ is reduced solutions resemble the piece-wise uniform case shown in Figure 6.2(a). Here we plot numerical solutions for the activator $v(\xi, t)$ with the *tanh* function for the domain growth and $\rho_1 = 0.001$, $\rho_2 = 0.0011$ and $\Theta = 0.5$. The initial domain length $\gamma_0 = 1$ and we plot solutions for (a) $\epsilon = 0.1$, (b) $\epsilon = 0.01$ and (c) $\epsilon = 0.001$ giving successively better approximations to the piece-wise uniform case.

similar to the uniform case (Figure 6.2(b)). As S becomes steeper then certain peaks fail to split at successively lower values of t (at correspondingly lower pattern modes).

Simulations for larger initial domains are shown in Figure 6.7, where we plot activator solutions for decreasing ϵ. We recover the piece-wise uniform behaviour, corresponding to Figure 6.4(a), as $\epsilon \to 0$. These results indicate that the transition from two activator peaks to three on the growing domain, when only the peak in the faster-growing region splits, is not strongly dependent on the exact nonuniformity. When $\epsilon \sim 1$, $S > 0$ on almost every part of the domain. We would expect splitting to be possible on the left-hand part of the domain except when ϵ is sufficiently small that $S \approx 0$ there. This is supported by the results in Figure 6.7 where it is only for very small ϵ that the splitting is restricted to the growing right-hand region, and not the left, as seen for the piece-wise uniform case.

Next we use the same model formulation to investigate reactant-controlled domain growth by choosing the local growth be a function of the local concentration of one or both of the reactants (the chemical species u or v).

6.1.4 Reactant-Controlled Growth. In this section we illustrate that the Lagrangian formalism may be used when explicit functional dependence for S on X and t is unknown, but rather S is a function of the dependent variables u and v. This will also be the appropriate formulation for numerical solution of the equations when S is determined by some extended system of constitutive laws describing the tissue growth. In the literature several models have been proposed in which domain growth is determined by reaction-diffusion variables. Dillon and Othmer [27] study pattern formation in the growing limb bud, modelled as an incompressible fluid with a distributed source term, S, which is a function of the local chemical composition. In their

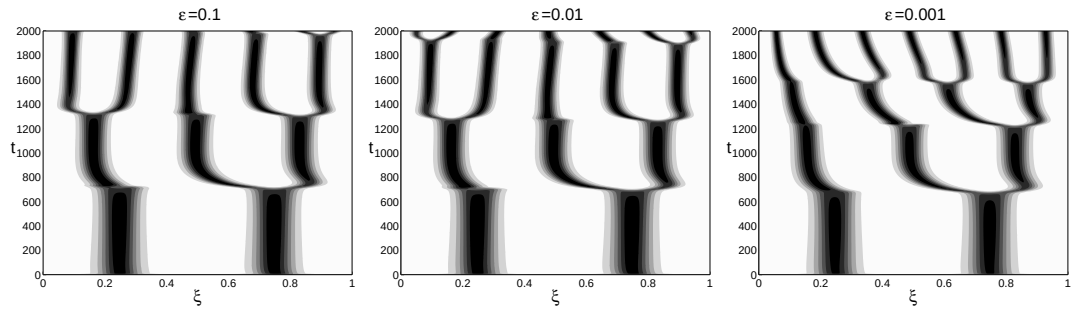

FIGURE 6.7 Pattern formation under nonuniform domain growth for larger initial domains. Numerical solutions are shown for the activator $v(\xi, t)$ with the *tanh* function for the domain growth and $\rho_1 = 0$, $\rho_2 = 0.001$ and $\Theta = 0.5$. The initial domain length is $\gamma_0 = 20$ and we plot (a) $\epsilon = 0.1$, (b) $\epsilon = 0.01$ and (c) $\epsilon = 0.001$.

model there are two chemical components which react and diffuse through the growing fluid region, however, their system is not of Turing-type and only simple gradients in the chemicals are formed. Modelling the morphogenesis of certain species of green algae, Harrison and coworkers [48, 50] couple a reaction-diffusion mechanism, which does generate Turing patterns, to domain growth. However, they also include a feedback mechanism to the kinetics such that DDI operates only within history-dependent boundaries separated by 'inert' regions for which there is no pattern formation.

The coupling of domain growth to the chemical kinetics provides a feedback between the pattern formation process and the mechanism that generates sequences of patterns. As an example, we consider a model for which domain growth is controlled by 'growth factor' v, the self-activating component, for which the reaction-diffusion dynamics are governed by

$$u_t = \frac{1}{\gamma_0}\frac{1}{\Gamma_X}\left[\frac{1}{\Gamma_X}u_X\right]_X + f(u,v) - u\,S(v) \tag{6.32}$$

$$v_t = \frac{d}{\gamma_0}\frac{1}{\Gamma_X}\left[\frac{1}{\Gamma_X}v_X\right]_X + g(u,v) - v\,S(v) - \Delta(v) \tag{6.33}$$

$$[\Gamma_X]_t = S(v)\,\Gamma_X \tag{6.34}$$

where $\Delta(v)$ is a function describing the uptake of the growth factor by the tissue and is a further modification to the reaction term for species v. We wish to consider reasonable forms for the uptake of v and the response function which determines the local growth $S(v)$. In biological systems such processes are governed by highly complicated biochemical pathways. We will not attempt to model these processes fully, rather we will assume a 'black box' type approach and assume functional forms which have reasonable properties.

The simplest approach is to assume that the uptake of growth factor by the tissue is proportional to its concentration. Then for constant tissue (cell) density the uptake will be a linear term in v. However, if the chemical binds to cell-surface receptors then the signal received by the cell will be saturating at high concentrations. If the inactive receptor R_i binds chemical C to form active receptor R_a then the rate equation for binding is

$$R_i + C \underset{k^-}{\overset{k^+}{\rightleftharpoons}} R_a \tag{6.35}$$

with rate constants k^+ and k^-. The Michaelis-Menten form for the fraction of bound (active) receptors F_b is given by

$$F_b = \frac{r_a}{r_a + r_i} = \frac{c}{\kappa + c} \tag{6.36}$$

where r_a and r_i are receptor concentrations (or densities) and $\kappa = k^-/k^+$ is the Michaelis-Menten constant. If binding of c to the receptors is cooperative then the sigmoidal expression for the bound fraction will contain the concentration c raised to the power m, reflecting the degree of cooperativity. In this case the uptake, with constant of proportionality α, is given by

$$\Delta(v) = \frac{\alpha v^m}{\kappa + v^m}. \tag{6.37}$$

The response of the cell to the fraction of bound receptors is far from trivial, involving complex signalling and intracellular machinery in the translation from chemical signal to cell growth and proliferation. A similar problem arises in the biological chemostat (or continuously-stirred tank reactor, CSTR, see for example Smith and Waltman [123]). In this experimental apparatus nutrient is supplied to a well-mixed tank containing a micro-organism population (with possibly several interacting species) and the run-off monitored to determine the rate of uptake of nutrient. This information, tallied with the population density increase, provides an empirical relationship between population growth and nutrient uptake. Here it has been noticed (Monod [84]) that the consumption of nutrient has the same sigmoidal relationship to the amount of nutrient supplied, and that the response of population growth is proportional to the uptake of the nutrient. The physiology of microbial uptake of nutrient and growth is a undoubtedly very complicated, however, the empirical sigmoid appears to be a remarkably good approximation, suggesting that the uptake is the limiting process involved. Similarly, in the absence of other detailed information, we suggest that the binding of the growth factor may in this respect be the important process for the tissue growth problem, and so we will assume a sigmoidal form for the local growth rate (in one spatial dimension) $S(v)$. Thus we suppose that the cellular interpretation of the number of bound receptors is proportional to the bound fraction.

The key features for this response function are the monotonicity and saturation of the sigmoid. In fact certain factors may produce non-monotonic response, for example

if a nutrient is essential at low concentration but inhibiting to growth (or toxic) at higher concentration. This is studied for the chemostat by Butler and Wolkowicz [11] and by Wolkowicz and Lu [132]. A similar biphasic response is observed in phototaxis for algae which are attracted toward sources of light but repelled by strong light [129]. The sigmoid dependence is also found in the chemotaxic response of certain organisms as the function that determines the bias in the random walk [61], the so-called receptor law [120, 102].

The assumption that tissue density remains constant implies that the result of tissue growth, increased cell size or proliferation, is expansion of the domain. The growth factor is removed sigmoidally (uptake) and the domain growth is then sigmoidal in response (proportional) with some delay, the time taken for the cellular response to produce new tissue, and the local growth S is given by

$$S(X,t) = S\big(v(X,t-\tau)\big) = \frac{\rho v(X,t-\tau)}{\kappa + v(X,t-\tau)}. \tag{6.38}$$

For simplicity we will assume that there is no delay, $\tau = 0$, so that tissue growth in response to the bound chemical is instantaneous. Although physically unrealistic, this approximation is reasonable in the context of reaction-diffusion patterns given that the solution is for the most part in quasi-steady state. Also we assume that ρ, which determines the ratio between the fraction of bound receptors and the growth rate (rather than biomass produced, as for the chemostat), will be small, so that domain growth remains *slow* in the sense that we have discussed. Furthermore, it is reasonable to assume that only a small amount of the growth factor is taken up by the receptors, so that the constant of proportionality α is also small. Finally, therefore, we consider the model

$$u_t = \frac{1}{\gamma_0}\frac{1}{\Gamma_X}\left[\frac{1}{\Gamma_X}u_X\right]_X + f(u,v) - \frac{\rho u v}{\kappa + v} \tag{6.39}$$

$$v_t = \frac{d}{\gamma_0}\frac{1}{\Gamma_X}\left[\frac{1}{\Gamma_X}v_X\right]_X + g(u,v) - \frac{(\rho v + \alpha)\, v}{\kappa + v} \tag{6.40}$$

$$[\Gamma_X]_t = \frac{\rho v}{\kappa + v}\,\Gamma_X. \tag{6.41}$$

We have solved this system numerically using the same computational routine as for the general nonuniform domain growth problem. The Lagrangian framework is preferred as it does not require explicit calculation of the local kinematic velocity for the domain, involving the inversion of Γ. A typical numerical solution for the activator species is shown in Figure 6.8(a), where the solution is interpolated to equally spaced points in ξ. The value of the local growth rate S is plotted as a function of time and scaled space in Figure 6.8(b), where those parts of the domain which are growing are shaded dark, and are seen to correspond closely to the evolving activator profile. The trajectories of particles embedded in the domain (flow lines) are plotted in Figure 6.9,

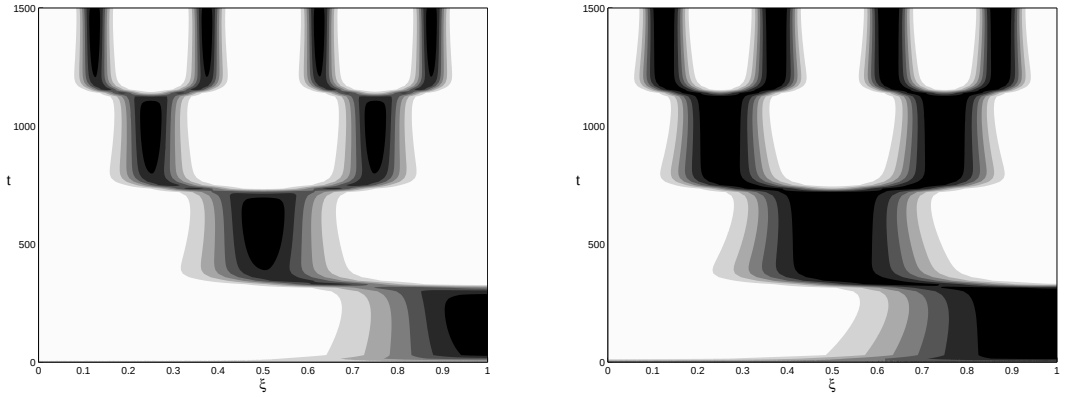

(a) (b)

FIGURE 6.8 Pattern formation with reactant-controlled domain growth. We plot (a) the activator (the 'growth factor') solution on the scaled domain and (b) the local strain rate (rate of volumetric change), for Schnakenberg kinetics and with $\gamma_0 = 1$, $d = 0.01$, $\rho = 0.005$ and $\kappa = 1$. We have taken $\alpha = 0$ although we have found no qualitative change to the results for small non-zero α. The numerical mesh has 1000 space points and no change to the solution is found by halving the mesh size.

uniformly scaled to the unit interval, given by

$$Z_X(t) = \Gamma(X,t)/\Gamma(1,t) \tag{6.42}$$

which we plot for different values of X. For clarity twice as many lines are plotted for $X \in [1/2, 1]$ as for $X \in [0, 1/2]$. In the figure the relative expansions of different regions of the domain are clearly seen. Numerical solutions were also computed with sigmoidal response functions for higher cooperativity, $m > 1$, giving qualitatively similar results.

The pattern sequence that is recovered is frequency-doubling in nature, through regular peak splitting (for the Schnakenberg kinetics). This result is perhaps unsurprising as the growth has the same symmetry as the pattern. However, this example illustrates that coupling between the domain growth and the reaction-diffusion pattern itself is sufficient to drive formation of the FD pattern sequence.

6.1.5 Discussion. The simulations presented in this section have all considered Schnakenberg kinetics, and pattern transitions have been through splitting of existing peaks in the solution profile. Naturally, similar results may be obtained for kinetic schemes for which transitions are through the insertion of new peaks. There is no significant effect on pattern amplitude or wavelength from the spatial dependence of terms in the equation for nonuniform growth. When domain growth is slow the advective term is correspondingly small, and peaks in the activator concentration reorganise continuously to maintain separation which is roughly independent of position. In Figures 6.1 and 6.3 the asymmetry in the pattern is due to the relatively high value of ρ. Here peaks do not reach their stationary positions during separation subsequent

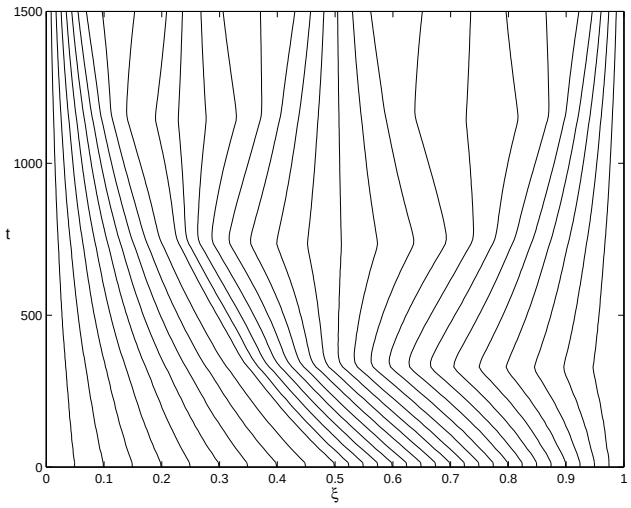

FIGURE 6.9 Flow lines, $Z_X(t)$, for reactant-controlled domain growth. The lines represent the trajectories of particles initially separated at regular intervals in X. For clarity twice as many points are taken in the second half as in the first half of the interval $X \in [0, 1]$. Parameters and other details as in Figure 6.8.

to splitting, before the domain is sufficiently large for the peaks to undergo the next transition. For slower domain growth (Figures 6.2 and 6.4) the nonuniformity of the domain growth is reflected in the failure of some peaks to split, giving an asymmetric sequence of patterns.

We have employed the Lagrangian formulation for nonuniform growth, and have described the numerical solution of the equations. However, the calculations proceed on a grid which is equally spaced in X, while patterns are approximately equally spaced in ξ. During growth of regions of the domain, any particular interval in X may expand to become a large interval in ξ. Hence in order to achieve reliable results a large number of grid points may be required. This is the trade-off against the computational effort saved in not being required to invert Γ during the calculation. In the simulations presented we have in each case performed computations with twice the number of grid points as shown, to ensure that the simulation has converged onto the true solution. A more sophisticated approach might be to periodically refine the computational mesh, to take the variable regional expansion into account.

We now reassess the two questions that were posed at the beginning of the chapter. We have shown that for small spatial perturbation, which we interpret as gentle gradients in the spatial dependence, we recover FD-type sequences (at least for the low modes that we have monitored). For more *strongly* nonuniform growth (for steeper change in S) at high ρ we have observed asymmetry, as for the uniform case, and for lower ρ selected peaks fail to undergo transitions, akin to the failure of FD for uniform linear growth. For highly nonuniform domain growth, and in particular when one region of the domain is not growing, other sequences may be formed by the failure of peak splitting (or insertion) at particular locations, specifically for those peaks on the

stationary part. This mechanism also appears to some degree robust, suggesting that it may be possible to choose the nonuniformity such that a specific pattern is selected during domain growth (as part of an evolving sequence) and furthermore, that the same pattern will be selected for some amount of variation of the nonuniformity.

6.2 Pattern Formation in Higher Dimensions

Much experimental research on biological and chemical pattern formation concerns patterning on surfaces or in relatively thin sheets. Correspondingly, in the literature concerned with biological problems as well as in chemical and physical systems there is a vast amount of work on theoretical aspects and modelling of pattern formation in higher spatial dimensions. Murray [88] considers reaction-diffusion as a model for animal coat markings and discusses linear stability and some effects of domain geometry on pattern formation. Meinhardt [82] discusses pattern formation in two dimensions in models for various aspects of embryology. Much of the work on pattern formation in chemical and physical systems centres around describing the detailed bifurcation structure near to the point of instability. The book by Walgraef [130] typifies this approach, discussing the use of amplitude equations to generate bifurcation diagrams near onset of instability in two spatial dimensions and in the investigation of the dynamics and properties of defects in the patterns. In a similar vein the article by Cross and Hohenberg [21] presents a wide review of pattern forming instabilities, including reaction-diffusion equations, as studied by amplitude and phase equations, including physically relevant aspects such as imperfections and issues related to pattern selection.

The major new feature for pattern formation in two dimensions is the influence of the geometry of the domain, and the conditions applied on the closed curve which bounds it. The increase in the number of spatial degrees of freedom gives rise to a corresponding escalation in the pattern selection problem, and hence pattern robustness. Kauffman *et al.* [59] considered pattern formation on the ellipse in reference to segmentation of the Drosophila embryo early in its development, and the sequential compartment formation in Drosophila wing disks, aiming to show that linear reaction-diffusion theory could account for the experimentally observed patterns in gene expression. Bunow *et al.* [10] have disputed these modelling results showing the strong sensitivity of the patterns to the precise geometry of the domain.

For reaction-diffusion systems, diffusion-driven instability may be studied in two dimensions with linear stability analysis of the homogeneous steady state, as for the one-dimensional case presented in section 2.2. The analysis proceeds as before, however the linear spatial modes are now eigenfunctions of the Laplacian in the higher spatial dimension, satisfying the conditions imposed on the domain boundary. The planforms of these patterns are discussed below (see also the book by Murray [88] for a full discussion).

There has been some work on pattern formation on curved surfaces. In his original paper on DDI, Turing discusses pattern formation on the sphere in the context of gastrulation. Recently Varea *et al.* [128] have studied pattern formation on the sphere and Chaplain *et al.* [14] have considered this problem in the context of solid tumour growth.

There are also some interesting results for three-dimensional chemical patterns (see Callahan and Knoblock [12] for a group theoretic analysis of pattern formation in three dimensions). Some general analytical results and concrete numerical simulations for three-dimensional patterns (and competition between modes) are presented by De Wit *et al.* [24]. So-called 'black-eye' patterns, which exhibit a hexagonal symmetry where the repeated element is a bright ring (surrounding a darker black-eye), have been observed in chemical reactors and it has been suggested by Gomes [42] that these apparently two-dimensional patterns in fact result from the projection of a three-dimensional lattice in a thin domain, viewed at the requisite orientation. Such patterns are observed elsewhere in nature and so these results may have implications for biological pattern formation.

In the present work we restrict discussion to the rectangular domain,

$$\Omega = [0, L_x] \times [0, L_y] \,, \tag{6.43}$$

and consider only growth in directions parallel to the axes of the rectangle. This is, of course, a great simplification but will serve to illustrate how the results we have obtained in one dimension extend to the higher dimensional problem. The nondimensionalised reaction-diffusion system on a domain of fixed size is given by

$$u_t = \frac{1}{\gamma}\nabla^2 u + f(u,v) \tag{6.44}$$

$$v_t = \frac{d}{\gamma}\nabla^2 v + g(u,v) \tag{6.45}$$

defined on

$$\overline{\Omega} = [0,1] \times [0,\alpha]$$

with zero flux boundary conditions imposed on the closed curve

$$\mathbf{x} \in \partial\overline{\Omega} \tag{6.46}$$

where $\gamma \propto L_x^2$ and $\alpha = L_y/L_x$ is the ratio of the sides of the rectangle.

Linear Analysis. The linear analysis presented in Chapter 2 may be extended to two-dimensional domains with boundary conditions prescribed on the bounding curve $\partial\overline{\Omega}$. We seek solutions to the spatial eigenvalue problem

$$\nabla^2\phi + k^2\phi = 0 \tag{6.47}$$

where $\phi(x,y)$ satisfies the boundary conditions on $\partial\overline{\Omega}$ and $k = |\mathbf{k}|$ is the magnitude of the wavevector of the linear mode (the dimensionless wavenumber). On the plane

the general form of solutions in which we are interested is

$$\phi_k(x,y) = \mathcal{R}e \sum_{j=1}^{M} A_j \exp\left(i\,\mathbf{k}_j \cdot \mathbf{x}\right) \tag{6.48}$$

to which solutions come in pairs for each j with wavenumbers $\pm k$, where $|\mathbf{k}_j| = k$. For $M = 1$ patterns are essentially one dimensional and we recover stripes (rolls) perpendicular to wavevector $\mathbf{k}$ and, for the isotropic case on the plane, with arbitrary orientation. For $M \geq 2$ periodic planforms may be generated, built on superposition of the pairs of wavevectors at angles which are multiples of π/M. Rhombic planforms may be produced, for which the wavevectors do not intersect perpendicularly.

When boundary conditions are imposed on the rectangular domain only a discrete set of wavenumbers is admissible. The exploration of the dispersion relation and determination of characteristic spatial scales in sections 2.2.4 and 2.3.1 may be extended similarly, i.e. k must lie in some interval $k \in [k_-, k_+]$ which may be determined from the dispersion relation, and a minimum domain size may be calculated for a particular linear mode. For $M = 1$ the directional degeneracy is eliminated, and we must have $\mathbf{k} \cdot \mathbf{x} = kx$ or ky, corresponding to stripes parallel to one or other axis. There are two cases of interest for $M = 2$, giving different planform orientations: firstly solutions that we will refer to as p-type, for which $A_1 = A_2 = a_k/2$ and

$$\mathbf{k}_1 \cdot \mathbf{x} = k_x x + k_y y, \quad \mathbf{k}_2 \cdot \mathbf{x} = k_x x - k_y y \tag{6.49}$$

such that the spatial eigenfunction may be written

$$\phi_k(x,y) = a_k \cos\left(k_x x\right) \cos\left(k_y y\right) \tag{6.50}$$

with $k_x = m_x \pi$, $k_y = m_y \pi/\alpha$ and $k^2 = k_x^2 + k_y^2$ giving a diagonal lattice of spots, and secondly s-type patterns,[2] where

$$\mathbf{k}_1 \cdot \mathbf{x} = k\,x, \quad \mathbf{k}_2 \cdot \mathbf{x} = k\,y \tag{6.51}$$

and from the boundary conditions $k = m_x \pi = m_y \pi/\alpha$, which gives a square planform which intersects the axes perpendicularly. The latter planform is admissible as a solution of the linearised problem when the domain may be tessellated by a square tile of appropriate size, for which a lower bound is determined by the minimum domain length calculated from the dispersion relation. For $M = 3$ the planform is hexagonal and corresponds to a hexagonal lattice of spots or a honeycomb structure. These structures cannot satisfy the zero flux boundary conditions on the rectangular domain. However, in the full nonlinear problem defects in the pattern allow distortion of the planform such that the boundary conditions may be satisfied. This is increasingly true for larger aspect ratio situations (the ratio of the domain size to the intrinsic pattern wavelength). Similarly, in the nonlinear regime the square planform may be distorted to give a rectangular lattice to satisfy the boundary conditions.

[2] We use the notation $m = [m_x, m_y]_p$ for p-type solutions and $m = [m_x, m_y]_s$ for s-type patterns.

Linear analysis does not give any insight into pattern selection between these different planforms. The relative stabilities of these bifurcating solutions are studied in the weakly nonlinear regime by amplitude equations that describe the evolution of the A_j as functions of time. These equations, derived by asymptotic expansion about the bifurcation point, are strictly valid only in the vicinity of the bifurcation. Nevertheless, good insight into the competition between different patterns can be gained by studying these equations and there is now a large literature concerning the bifurcation structures characterising different models and, more recently, in reproducing phenomena from the experimental Turing patterns. In two dimensions, consideration of solutions to the amplitude equations generated for one, two or three interacting destabilising modes allows one to find the relative stabilities of bifurcating stripe, square and hexagonal symmetric structures. Furthermore, amplitude equations may be used to examine the dynamics of defects in patterns and the transitions to more stable patterns (for example, Eckhaus and zigzag instabilities [21, 130]). A generic result for many reaction-diffusion systems, such as those studied here, is that hexagons appear first in a subcritical bifurcation, and then lose stability to squares or stripes depending on the relative size of the quadratic and cubic terms in the reaction kinetics.[3] It is now well documented that quadratic terms favour squares and hexagonal patterns over stripes. The competition between striped and spotted patterns (squares or hexagonal planform) has been investigated by Ermentrout [37] and Lyons and Harrison [74, 75] where it is shown that quadratic terms favour spots. Some numerical results supporting this conclusion are presented below. We will consider the Schnakenberg system, the quadratic nature of which becomes apparent after expanding the reaction terms around the kinetic steady state (see Appendix A.1), for which the solution on a fixed domain is shown in Figure 6.13(d), and we take the cubic autocatalysis model from Chapter 5 as a canonical stripe-generating system, showing the solution on a fixed domain in Figure 6.14(c).

6.2.1 Numerical Solution in Two Dimensions. The reaction-diffusion model in two dimensions can be solved numerically using standard methods for parabolic equations on rectangular grids (see Morton and Mayers [85]). The simplest finite difference method is the fully explicit Euler scheme which works well enough but, as in one spatial dimension, is subject to a prohibitively restrictive stability condition. In one dimension this restriction is circumvented by the semi-implicit Crank-Nicolson scheme, which gives a linear system of near-tridiagonal form which is easily (and inexpensively) solved. However the direct extension of this scheme to two dimensions results in the loss of the tridiagonality of the matrix equation to be solved, which greatly slows down the computation. The tridiagonal form is retained by the *Alternating-Direction Implicit* (ADI) scheme of Peaceman and Rachford [108] for which the integration is

[3] The relevant nonlinear terms here are those found by expanding the functions about the kinetic steady state concentration values—see section 5.2.

explicit in one direction and implicit in the other for one half-timestep, and for the second half-timestep the order is reversed.

We seek a numerical solution on the spatial grid (x_i, y_j) with $x_i = (i-1)\Delta x$, $i = 1, \ldots, N_x$ and $y_j = (j-1)\Delta y$, $j = 1, \ldots, N_y$, where $\Delta x = \Delta y$ for a uniform grid, and time $t_k = k\Delta t$, $k = 0, 1, 2, \ldots$ with timestep Δt. For numerical approximation $U_{i,j}^k \approx u(x_i, y_j, t_k)$ we have

$$\left[1 - \frac{\Delta t}{2\,(\Delta x)^2}\,\delta_x^2\right] U_{i,j}^{k+1/2} = \left[1 + \frac{\Delta t}{2\,(\Delta y)^2}\,\delta_y^2\right] U_{i,j}^k + \frac{\Delta t}{2} f\left(U_{i,j}^k, V_{i,j}^k\right) \tag{6.52}$$

$$\left[1 - \frac{\Delta t}{2\,(\Delta y)^2}\,\delta_y^2\right] U_{i,j}^{k+1} = \left[1 + \frac{\Delta t}{2\,(\Delta x)^2}\,\delta_x^2\right] U_{i,j}^{k+1/2} + \frac{\Delta t}{2} f\left(U_{i,j}^{k+1/2}, V_{i,j}^{k+1/2}\right) \tag{6.53}$$

where $\delta_x U_{i,j}^k = U_{i+1/2,j}^k - U_{i-1/2,j}^k$ is the central difference operator, and a similar expression holds for δ_y. An equivalent formula gives the numerical approximation $V_{i,j}^k \approx v(x_i, y_j, t_k)$.

The resulting scheme is unconditionally stable (as for the Crank-Nicolson scheme), although there is still a condition for convergence [85]. The tridiagonal linear system of equations is efficiently solved using LU decomposition (see Press *et al.* [113]).

6.3 Two-Dimensional Slow Uniform Domain Growth

We restrict our attention to uniform domain growth, where the strain rates are independent of position, although we may allow different rates along the two axes to give anisotropic domain growth, which is specified by

$$\mathcal{D}_{ij} = \delta_{ij}\sigma_i(t), \qquad i = 1, 2 \tag{6.54}$$

(no summation implied) where $\sigma_1 \neq \sigma_2$ for anisotropic uniform growth. Transforming the rectangular growing domain to the unit square,

$$(x, y) \to (\xi, \eta) = \left(\frac{x}{r_1(t)}, \frac{y}{r_2(t)}\right) \tag{6.55}$$

where

$$r_i(t) = \exp \int_0^t \sigma_i(\bar{t})\,\mathrm{d}\bar{t} \tag{6.56}$$

such that $\Omega = [0, 1] \times [0, 1]$, we recover the equations

$$u_t = \frac{1}{\gamma(t)}\left(u_{\xi\xi} + \frac{1}{[\alpha(t)]^2} u_{\eta\eta}\right) + f(u, v) - S(t)u \tag{6.57}$$

$$v_t = \frac{d}{\gamma(t)}\left(v_{\xi\xi} + \frac{1}{[\alpha(t)]^2} v_{\eta\eta}\right) + g(u, v) - S(t)v \tag{6.58}$$

where we define

$$\gamma(t) = \gamma_0\,[r_1(t)]^2 \quad \text{and} \quad \alpha(t) = \alpha_0 \frac{r_2(t)}{r_1(t)} \tag{6.59}$$

so that $\alpha(t)$ is the time-varying ratio of the sides, and $\alpha_0 = L_y/L_x$ is the initial ratio. The rate of volume expansion S is given by

$$S(t) = \sigma_1(t) + \sigma_2(t). \tag{6.60}$$

In light of the results presented in previous chapters for pattern sequences on the growing one-dimensional domain, two central issues must be resolved for the model in two dimensions:

1. Do the one-dimensional results hold for two-dimensional domains undergoing *uniaxial* domain growth: does the splitting and insertion of peaks observed in the one-dimensional study have an analogous behaviour for the two-dimensional problem, or does the higher dimensionality destroy the sequences of patterns?
2. What qualitative changes occur for *biaxial* growth in two-dimensions: what pattern sequences are formed and are the patterns robustly generated?

In the following section we present the results of numerical simulations of the model assuming various forms for the kinetics and with several choices of σ_1 and σ_2. The system is solved numerically using the ADI method described above, incorporating the relevant functional dependence for those parameters in the equations which change with time.

6.3.1 The Quasi-One-Dimensional Problem. Firstly we examine the pattern sequences generated on a narrow strip, with growth parallel to the long axis only (along the x-direction). Taking an initial domain with ratio of sides $\alpha < 1$ we set

$$\sigma_1(t) = \rho_1, \qquad \sigma_2(t) = 0 \tag{6.61}$$

where $\rho_1 \ll 1$ so that domain growth is slow. The numerical solution for the activator $v(x, y, t)$ is shown in Figure 6.10. The solution is plotted as a function of x and y at various times t, so that the changing shape of the domain with time is apparent. The reaction terms $f(u, v)$ and $g(u, v)$ in equations (6.57) and (6.58) were taken to be the spot-selecting Schnakenberg kinetics. The width of the strip (the y-extent) was taken to be half of the initial length. The solution shows the standard spatial frequency-doubling behaviour as was obtained for the one-dimensional studies presented above.

In this example the width of the domain is sufficiently small (and is unchanging) that the only admissible patterns are of zeroth mode in the y-direction: the patterns generated in the sequence are all of mode $m = [\,\cdot, 0]_p$. Thus there is no dependence of the solution on y, and the solution behaviour is truly one-dimensional.

6.3.2 Uniaxial Domain Growth. If we choose the initial domain geometry such that a genuinely two-dimensional pattern, one with spatial dependence on x and y, is established initially then we may examine how the pattern evolves under anisotropic growth (along one axis only). As in the previous case, we take $\sigma_1 = \rho$ and $\sigma_2 = 0$ such that the domain is growing parallel to the x-direction only, but here α is increased to give a wider elongating strip. In Figure 6.11 the domain is initially square, and

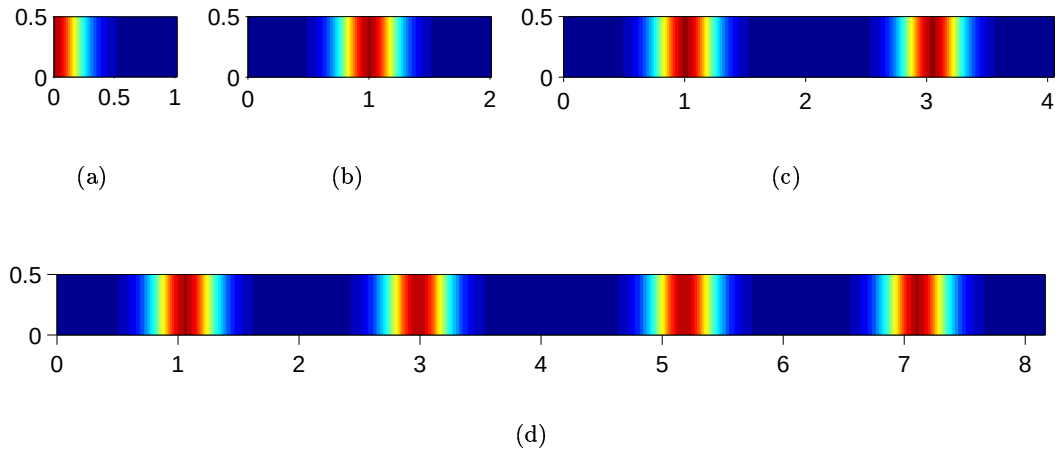

FIGURE 6.10 Spatial frequency-doubling via peak splitting for Schnakenberg kinetics on a thin elongating strip, with $\gamma_0 = 1$, $\alpha_0 = 0.5$ and $\rho_1 = 0.002$ ($\rho_2 = 0$). The activator solution $v(x, y, t)$ is shown at times (a) $t = 10$, (b) $t = 350$, (c) $t = 700$ and (d) $t = 1050$, corresponding to a doubling in x-extent at each step. Pseudo-colour scale is from 0 (blue) to 4 (red).

from random initial conditions with Schnakenberg kinetics the initial pattern to form is of mode $m = [+1, -2]_s$, equivalent to a half-spot, shown in 6.11(a). During the subsequent growth along the x-axis the solution evolves as a sequence of spot-patterns with rapid transitions between quasi-steady spatial profiles, comprising pattern modes $m = [+1, -2]_s$, $[-2, -2]_s$, $[-4, -2]_s$, $[-8, -2]_s, \ldots$. The sequence is generated in a similar manner to the pattern sequence in the one-dimensional case, with transitions by splitting and separation of the spots as the domain doubles in length in the x-direction.

The transition between two quasi-steady pattern modes is shown in detail in Figures 6.12(a)–(c). In Figures 6.12(d)–(h) the profile along the midpoint in y and parallel to the x-axis, $v(x, 1/2)$, is plotted for various times t corresponding to the full patterns in Figures 6.11(b), 6.12(a)–(c) and 6.11(c) respectfully. These graphs are strongly reminiscent of the peak-splitting phenomenon for solutions on the one-dimensional growing domain (Figure 4.6(a)–(d)), although it is interesting to note that the two-dimensional patterns have approximately twice the amplitude of the one-dimensional solutions.

In this example it is apparent that the domain remains too narrow to allow significant reorganisation of the arrangement of spots through relaxation into a different lattice type. Furthermore it is unclear whether the line of spots observed corresponds more closely to a narrow band along the axis of a square lattice or a similar thin strip along the vertices of a hexagonal planform. Further numerical simulations on domains of different initial size and geometry indicate that uni-directional growth favours the symmetry of the square lattice. In Figure 6.13(a) we have chosen the initial domain

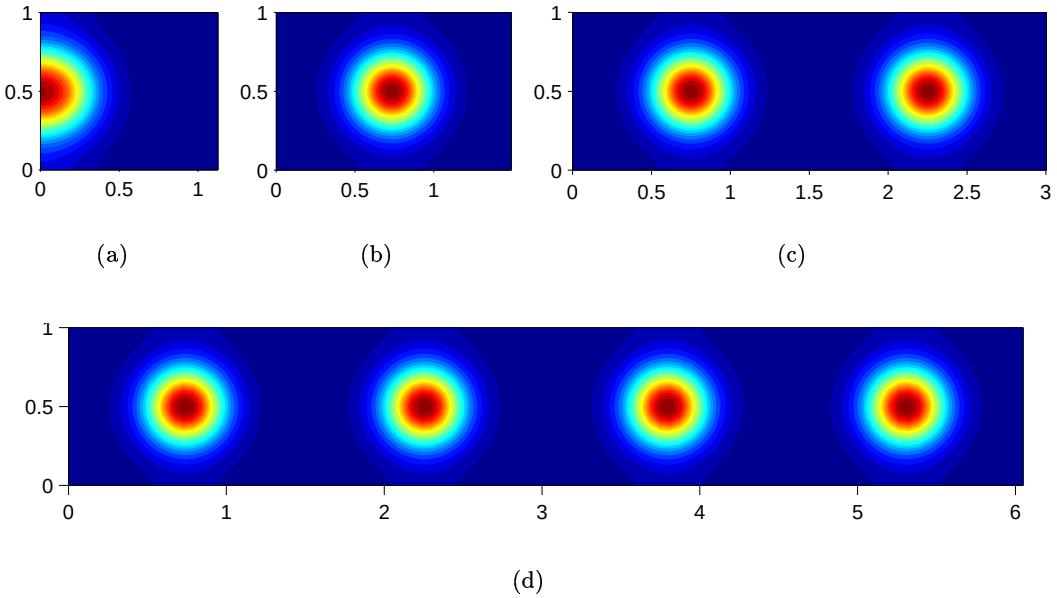

FIGURE 6.11 Spot splitting for Schnakenberg kinetics on an elongating strip, with $\gamma_0 = 1$, $\alpha_0 = 1$ and $\rho_1 = 0.002$ ($\rho_2 = 0$). We plot the activator pattern $v(x, y, t)$ at times (a) $t = 60$, (b) $t = 200$, (c) $t = 550$ and (d) $t = 900$, corresponding to doubling the strip length during the intervals between (b) and (d). In these and in subsequent spot-type patterns the pseudo-colour scale is from 0 (blue) to 8 (red).

length such that the destabilising pattern is mode $m = [-2, -6]_s$. For uniaxial domain growth along the x-axis the regular splitting of spots is found to occur, giving frequency-doubling in the x-direction, with the final pattern shown in Figure 6.13(b) after two such transitions. On this wider domain the arrangement of spots is not found to relax into a hexagonal lattice, the planform favoured on a static domain, which is shown in Figure 6.13(d). Here the fixed domain is of identical size and geometry to the growing domain at the time shown in the previous frame. The distortion of the hexagonal lattice is due to the relatively small aspect ratio, however, on larger fixed domains a truer hexagonal lattice is recovered, albeit with some defects to allow the boundary conditions to be satisfied.

Now we turn to examine pattern behaviour for kinetic schemes which select stripe patterns through dominance of the cubic terms in the expanded kinetics. As an example we take the system studied in detail in Chapter 5, with kinetics given by equation (5.26)–(5.27). Initially it will be our purpose to investigate whether, as in the previous example, domain growth can generate a pattern of greater symmetry than is generated on a static domain. For a small initial domain with $\alpha_0 > 1$ stripes preferentially align parallel to the shorter axis, as shown in Figure 6.14(a). Here the initial domain geometry is such that the first pattern to form is $m = [0, -6]_p$. During subsequent growth along the direction of the x-axis, such that at some later

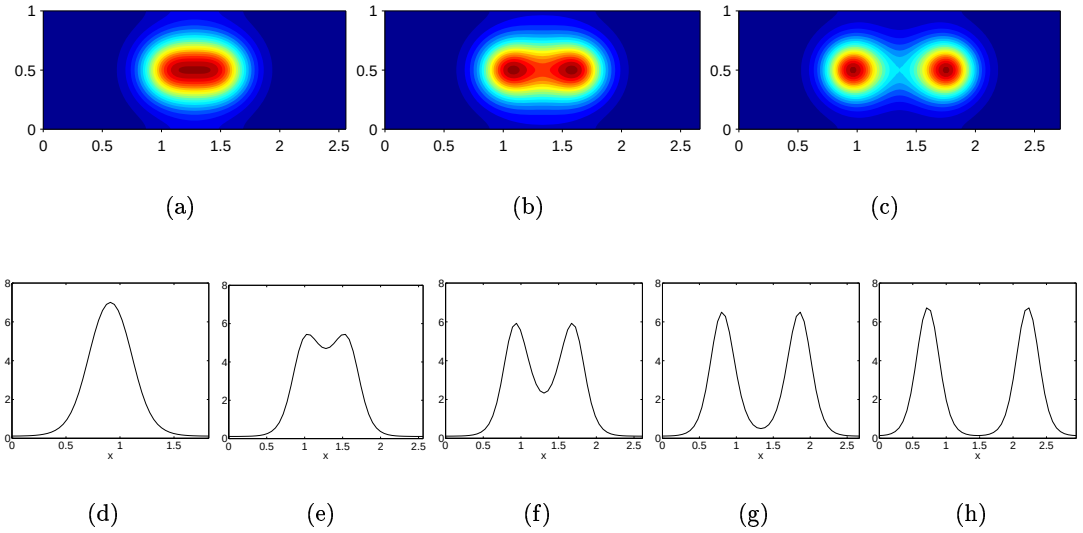

FIGURE 6.12 Detail of spot splitting for Schnakenberg kinetics, at times (a) $t = 470$, (b) $t = 480$ and (c) $t = 490$, and cross section profile, $v(x, 1/2, t)$, at times (d) $t = 200$, (e) $t = 470$, (f) $t = 480$, (g) $t = 490$, and (h) $t = 550$. Parameters as for Figure 6.11.

time the ratio of the sides $\alpha < 1$, the stripe pattern is essentially unchanged, shown in Figure 6.14(b). The pattern mode remains $m = [0, -6]_p$ although the size and geometry of the domain has changed significantly, as is reflected by the change of α where now $\alpha = 1/2$. In Figure 6.14(c) we show the activator solution generated from random initial data on a fixed domain of equal size and geometry to the previous frame. The intrinsic spatial scale (pattern wavelength) is clearly approximately the same, however, the simple symmetry of the pattern on the growing domain is not recaptured. Thus the effect of the uniaxial growth in this case is to stabilise a parallel stripe pattern. We have considered the kinetic system with small a positive quadratic term. Further simulations indicate that this behaviour is independent of the precise form of the kinetics, requiring only that stripes are strongly preferred. Variations on the kinetics with this proviso serve only to modify the cross-sectional profile of the stripes (which resemble the profiles for patterns on the one-dimensional domain).

6.3.3 Biaxial Domain Growth. In the previous section we examined the pattern sequences generated on a two-dimensional domain subject to growth along one axis only, and under various conditions on the domain geometry and reaction kinetics. Now we consider a two-dimensional rectangular domain with slow uniform domain growth along both axes, with

$$\sigma_1(t) = \rho_1, \qquad \sigma_2(t) = \rho_2 \tag{6.62}$$

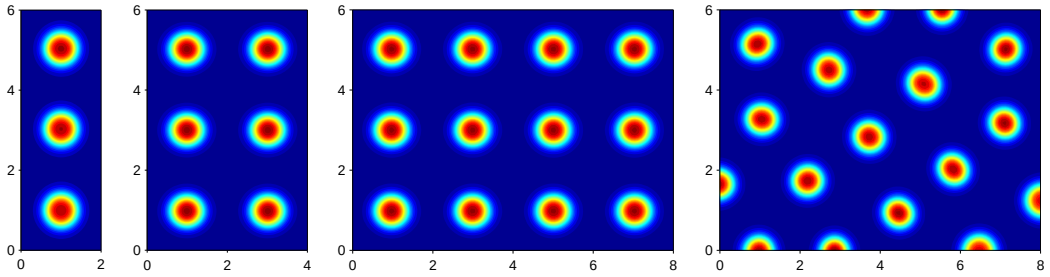

FIGURE 6.13 Selection of the square lattice through spot splitting on the uniaxially growing domain compared to the hexagonal lattice for pattern formation on a domain of fixed size. In (a)–(c) we plot activator solutions $v(x, y, t)$ for Schnakenberg kinetics on the growing domain with $\gamma_0 = 4$, $\alpha_0 = 3$ and $\rho_1 = 0.002$ at times (a) $t = 10$, (b) $t = 300$ and (c) $t = 650$. For (d) the domain is static ($\rho_1 = \rho_2 = 0$) and we plot a steady state pattern for $\gamma_0 = 64$ with $\alpha = 0.75$, giving the same domain size and geometry as (c).

where ρ_1 and ρ_2 are both small. When $\rho_1 = \rho_2$ the domain growth is isotropic. Within this same framework we could also assume some time dependence for the domain growth, as for several examples in Chapter 4.

Stripe Patterns. Firstly we reconsider stripe formation. Previously we found that stripes parallel to the direction of uniaxial growth remain aligned to the growth direction. However, of great interest is the stability of stripe patterns when domain growth is also in the direction perpendicular to the stripe orientation. Here elongation and separation of stripes occur simultaneously and, referring to the first question that we posed, the crucial issue is whether the stripes split in a manner similar to the one-dimensional problem (see Figure 5.3). The results of numerical simulations, presented in Figure 6.15, confirm this to be the case. In the figure the growth is isotropic, and so α retains its initial value, $\alpha_0 = 1$. Thus the vertices plotted are (ξ, η), showing the activator patterns $v(\xi, \eta, t)$ in the unit square, at various times t. The direction of a stripe pattern on a square domain will be parallel to one or other axis, the orientation determined by the initial data alone. In these simulations we use the cubic autocatalytic kinetic scheme (5.26)–(5.27) to study the subsequent evolution of striped pattern sequences under isotropic uniform domain growth.

In Chapter 5 it was shown that the perturbation of pure cubic kinetics with small quadratic terms determines whether evolving solution sequences on the one-dimensional domain gave rise to transitions through splitting or insertion of new peaks (or both simultaneously in the absence of the quadratic term). The same appears to be true for the transitions between pattern modes in two dimensions. In Figures 6.15(a)–(c) the sequence of patterns for the pure cubic case ($\delta = 0$) is shown. Here we see the

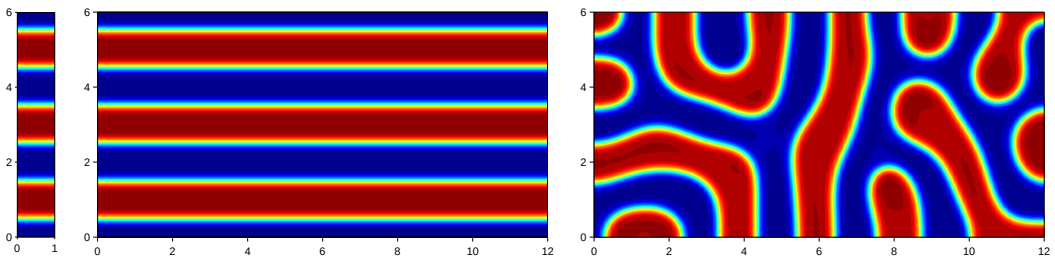

(a) (b) (c)

FIGURE 6.14 Domain growth parallel to stripes maintains the orientation of the striped pattern. Numerical solution for cubic autocatalysis kinetics with $\delta = 0.1$ on the uniaxially growing domain (a)–(b), compared with the steady state pattern generated on a fixed domain (c) of the same size as figure (b). Parameters for domain growth are $\gamma_0 = 1$, $\alpha_0 = 6$ and $\rho_1 = 0.005$ with final time (b) $t = 500$. In these and in subsequent stripe patterns the pseudo-colour scale is from -0.8 (blue) to 0.8 (red).

mode-tripling sequence that was described previously for the one-dimensional problem. The initial pattern is $m = [+1, 0]_p$, with subsequent patterns in the sequence $m = [-3, 0]_p$, $[+9, 0]_p, \ldots$, and with transitions each time the side perpendicular to the axis of the stripes triples in length. This sequence is the two-dimensional realisation of the frequency-tripling in the x-direction. In Figures 6.15(d)–(g) the kinetics are perturbed with a small positive quadratic term, such that stripes are selected but pattern transitions occur via insertion of new stripes each time the perpendicular side doubles in length, as for the one-dimensional case. Similar sequences are generated for anisotropic growth and for initially rectangular domains, where the ratio of the sides may bias the initial orientation of the stripe pattern. Painter [106] found, for one particular kinetic mechanism, that the parallel stripe structure may break down under domain growth, evolving to labyrinthine patterns. We have not observed similar behaviour here, and assume that the kinetic scheme that was used does not strongly select for stripes.

These results are simple two-dimensional extensions of the one-dimensional results discussed earlier. However, new phenomena emerge for the spot patterns under biaxial domain growth.

Spot Patterns. Using Schnakenberg kinetics we study the formation of spot patterns on isotropically growing domains, taking $\rho_1 = \rho_2$ for the domain growth rates (6.62). The pattern sequence for an initially square domain ($\alpha_0 = 1$) is shown in Figure 6.16. The novel feature demonstrated in this figure is the splitting of a single spot into four. As usual, spot splitting occurs when the axial length doubles. The symmetry of this sequence is certainly due to the square domain and the isotropic growth. If the domain is not square initially, or for anisotropic growth such that $\rho_1 \neq \rho_2$, then spot splitting events along the two perpendicular axes occur at different times. This

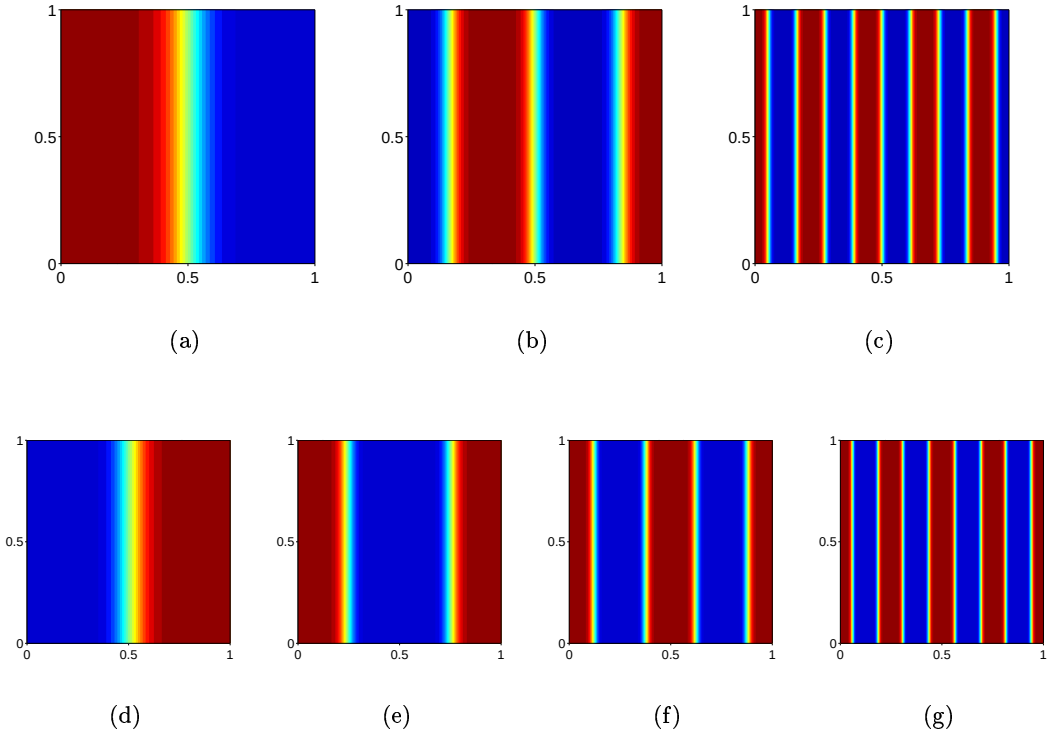

FIGURE 6.15 Sequences of stripe patterns generated under biaxial domain growth for cubic autocatalysis kinetics (5.26)–(5.27) showing (a)–(c) frequency-tripling of stripes for $\delta = 0$ and (d)–(g) frequency-doubling by stripe insertion for $\delta = 0.1$. The domain remains square as it grows, although this is not a requirement for the pattern sequences shown. The orientation of the stripes is in this case arbitrary, chosen by the random initial conditions. Similar behaviour is observed in the perpendicular orientation for stripes which are initially parallel to the x-axis. Parameters are $\gamma_0 = \alpha_0 = 1$ and growth rates $\rho_1 = \rho_2 = 0.002$ with solutions for the activator $v(\xi, \eta, t)$ shown on the scaled domain $[0, 1] \times [0, 1]$ at times (a) $t = 200$, (b) $t = 600$ and (c) $t = 1200$, and (d) $t = 250$, (e) $t = 600$, (f) $t = 950$ and (g) $t = 1300$. For plots (a)–(c) the domain sides triple and for (d)–(e) the sides double in length between each plot.

is because the axial length in one direction reaches its critical value before that of the other direction. The results of a numerical simulation for the latter of these two cases is shown in Figure 6.17. Here we plot $v(x, y)$ for various times t to show the changing shape of the domain. The domain is initially square but growth is faster parallel to the y-axis and spots separate more quickly in this direction. The figure illustrates that on removing the square symmetry the quadruple splitting is lost, however, the rectangular planform is retained.

Transitions between patterns for Schnakenberg kinetics are through splitting of peaks in one dimension, and spot splitting for two-dimensional patterns, the details of which depend on the symmetries in the domain and its growth. Details of the spot splitting are shown in Figure 6.12 and in Figure 6.16 for the square-symmetric domain. Alternative kinetic schemes which also select spot patterns were shown in one

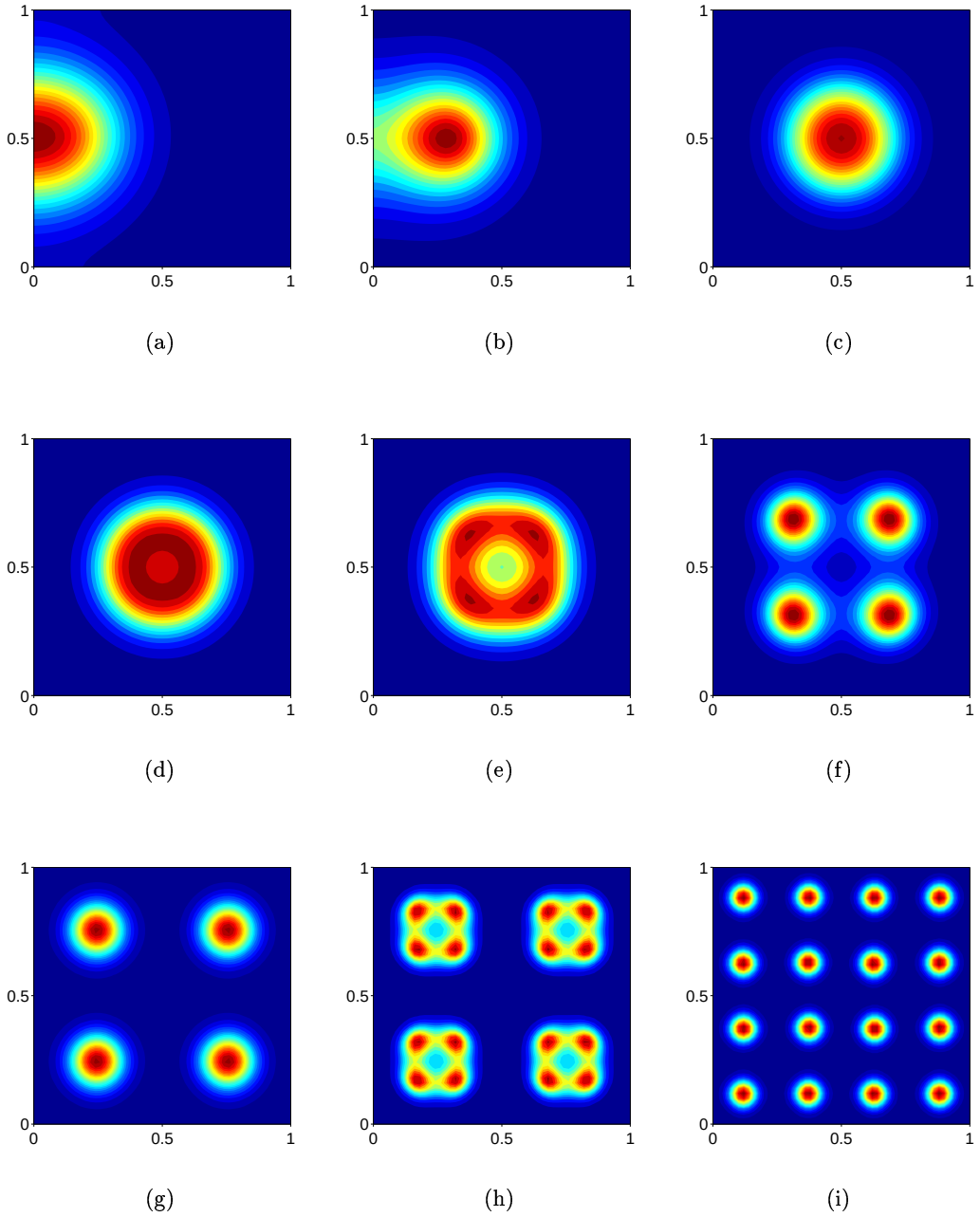

FIGURE 6.16 Symmetric splitting of spots generating a square lattice pattern for Schnakenberg kinetics on the isotropically growing domain. Parameters are $\gamma_0 = \alpha_0 = 1$ and growth rates $\rho_1 = \rho_2 = 0.002$ with solutions for the activator $v(\xi, \eta, t)$ shown at times (a) $t = 50$, (b) $t = 100$, (c) $t = 150$, (d) $t = 350$, (e) $t = 400$, (f) $t = 420$, (g) $t = 500$, (h) $t = 750$ and (i) $t = 850$. The domain length scale doubles between (c), (g) and (i).

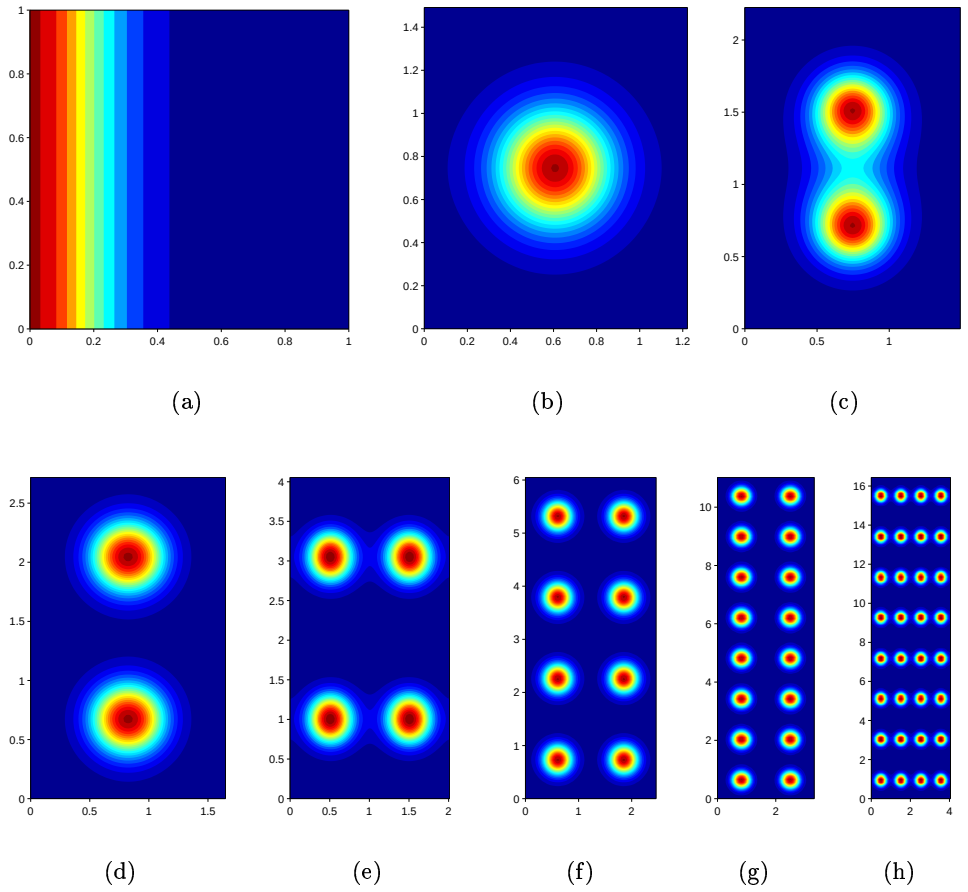

FIGURE 6.17 Generation of the rectangular lattice for Schnakenberg kinetics under anisotropic growth. Here $\rho_1 = 0.001$ and $\rho_y = 0.002$ while $\gamma_0 = \alpha_0 = 1$. The activator solution $v(x, y, t)$ is shown at times (a) $t = 10$, (b) $t = 200$, (c) $t = 400$, (d) $t = 500$, (e) $t = 700$, (f) $t = 900$, (g) $t = 1200$ and (h) $t = 1400$.

spatial dimension to undergo transitions via insertion of new peaks, the example we have used being the Gierer-Meinhardt equations (see Appendix A.3) with δ nonzero. In Figure 6.18 we plot the pattern sequence generated for Gierer-Meinhardt kinetics on an initially square, isotropically growing domain. Interestingly, a new phenomenon emerges for spot insertion. The patterns are found to alternate between two different orientations of the square lattice, what we have called p-type (diagonal) and s-type (square) planforms. For example in Figure 6.18(d) the pattern mode is $m = [+2, +2]_p$, which persists until the domain *side* is long enough to accommodate new peaks, at which point insertion of peaks generates mode $[+4, +4]_s$, shown in Figure 6.18(e). This mode, in turn, persists until the *diagonals* are long enough to accommodate insertion of new peaks, giving pattern mode $m = [+4, +4]_p$ (Figure 6.18(f)). This regular alternation takes place with time period corresponding an increase in the length of the domain side by a factor of $\sqrt{2}$. Thus between Figures 6.18(c) and 6.18(e), and

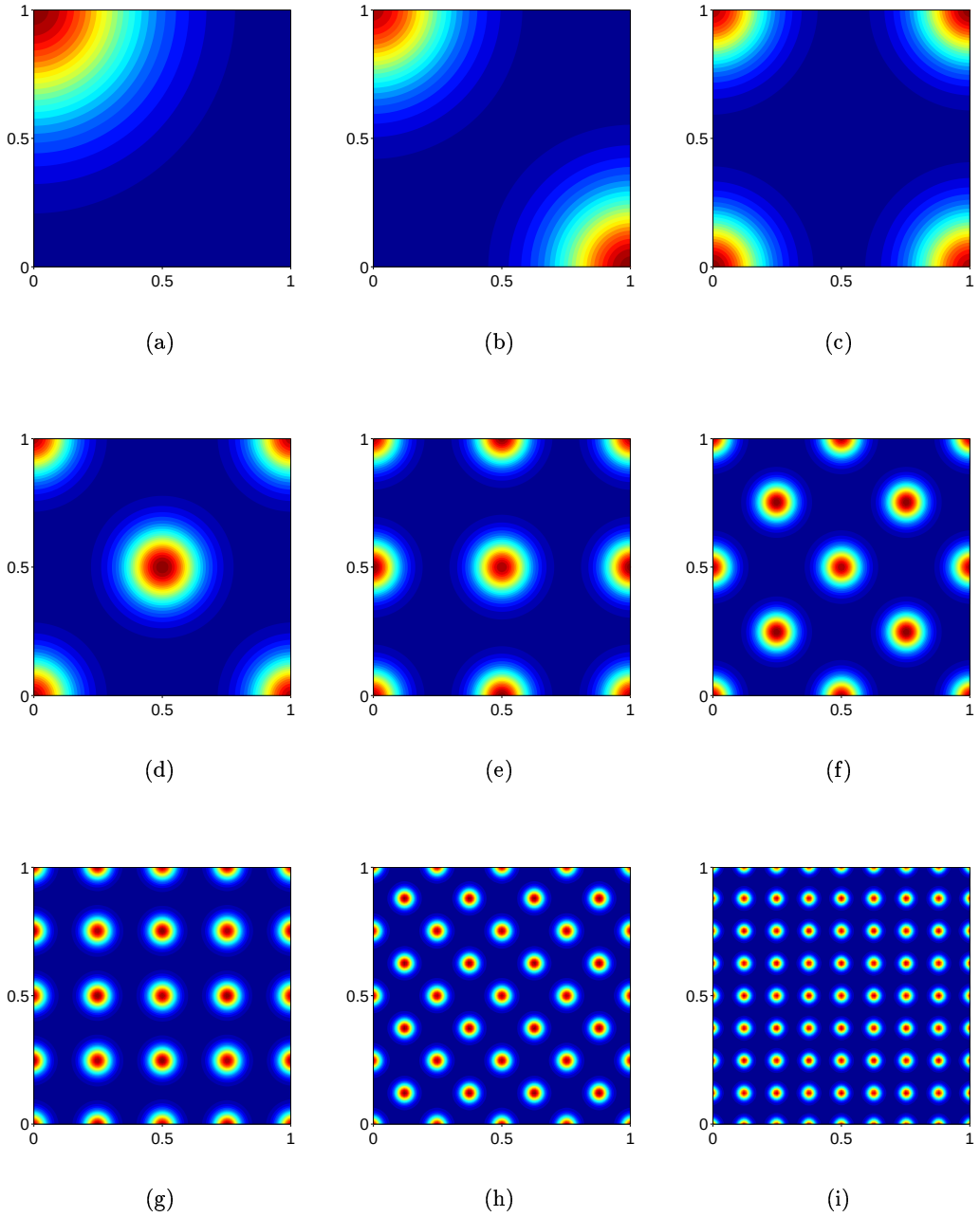

FIGURE 6.18 Spot insertion leading to alternation between orientations of the square lattice for Gierer-Meinhardt kinetics under isotropic domain growth. Between successive patterns the domain sides increase by a factor of $\sqrt{2}$. In this figure the ratio of diffusivities $d = 0.025$, and other parameters are $\gamma_0 = \alpha_0 = 1$ and $\rho_1 = \rho_2 = 0.005$. Numerical solutions for the activator $v(\xi, \eta, t)$ are shown at times (a) $t = 110$, (b) $t = 180$, (c) $t = 250$, (d) $t = 320$, (e) $t = 390$, (f) $t = 460$, (g) $t = 530$, (h) $t = 600$ and (i) $t = 670$.

between Figures 6.18(d) and 6.18(f) the domain sides and diagonals respectively double in length. Essentially there are two intercalating frequency-doubling sequences here, one sequence lagging the other. We have observed similar behaviour in numerical simulations on rectangular lattices, where the square symmetry and isotropic growth are relaxed (data not shown).

6.3.4 Discussion. These results indicate that pattern formation in two spatial dimensions can give rise to essentially one-dimensional pattern sequences, both for thin domains and for regular stripe patterns on squarer geometries. We have shown that domain growth may in fact stabilise parallel stripe patterns on domains of a size that would generate labyrinthine patterns for the static problem. Furthermore, we have shown that for spot-favouring kinetics the domain growth selects the square (or rectangular) lattice, rather than the hexagonal planform which is selected in the static case. An interesting observation for spike-type kinetics generating spot patterns is that the amplitude of the two-dimensional patterns is approximately twice that of one-dimensional structures. This is not the case for transition-layer systems where the amplitude is determined by the location of the two stable branches of the activator nullcline in the (u, v) plane.

The generation of patterns with increasing numbers of spots retaining the regular square symmetry is achieved when the initial domain is sufficiently small that regular patterns are generated initially. However, if the domain is initially large so that a disordered pattern forms initially (such as in Figure 6.13(d) or, for stripes, Figure 6.14(c)) then during subsequent domain growth the patterns do not relax to the regular lattice of spots (or to parallel stripe structures). In this sense the two-dimensional pattern sequences are unlike those observed in one dimension, where for exponential growth a frequency-doubling sequence will ensue from any initial pattern mode.

The preference for the square lattice seems to be generic for the different kinetic schemes and domain growth functions that we have considered. The higher symmetry afforded by square domains undergoing biaxial isotropic growth is certainly reflected in the pattern of peak splitting, viz. one peak splitting into four. This raises the interesting question of what patterns of peak splitting would be observed for other symmetries imposed on the domain geometry and growth. Lacalli [67] describes a numerical simulation of a reaction-diffusion equation on a circular disc with radially symmetric growth, where a central peak is found to split into six in a manner similar to the expanding ring which collapses into four peaks in Figure 6.16. However, the lattice generated under such symmetry is not reported. It is conceivable that the circular symmetry of radially symmetric growth will select the hexagonal planform. This is an interesting possibility which we have not yet explored, however, we would not expect the six-fold splitting to be recovered for perturbations of either the circular domain geometry or the radial symmetry of the growth.

The symmetry arguments presented in Chapter 2 for the steady state solutions and extended in Chapter 4 to the full PDE system hold equally well in two space dimensions. The transitions occur when the relevant spatial dimension doubles. However, for spot-inserting kinetics we have found a novel behaviour whereby two patterns exhibiting this symmetry intercalate. The pattern on the domain alternates between two different planforms as the domain grows. There are two important dimensions for the insertion mechanism due to the lattice structure, one parallel to the axes and the other the length of the diagonals. Insertions occur at the appropriate points, either midway between existing spots on lines parallel to the domain edges or on lines parallel to the diagonal, as these lengths double.

The results we have presented are confined to the highly restricted case of rectangular domains and growth out along one or both rectangular axes. Furthermore we have considered only growth at constant strain rate, and have not considered time dependence or indeed spatial nonuniformity in the growth. Time-dependence for the strain rates is easily incorporated into the numerical methods that we have discussed, and we would expect the results to be equivalent to those for the one-dimensional problem. In order to explore pattern formation on two-dimensional domains with more general geometries it is expedient to employ the finite element method for numerical solution of the equations, and this is currently under investigation [76]. Our formulation of the problem for numerical solution on rectangular domains may be extended to include nonuniform growth by writing the equations in Lagrangian form and modifying the numerical scheme to cope with convective terms, using an upwind method (see Morton and Mayers [85]).